



## OPEN Investigation on rub-impact response characteristics of gas generator rotor system under external excitation

Haibiao Zhang<sup>1,2,3</sup>, Tao Liu<sup>4</sup>✉, Haifeng Zhao<sup>3</sup> & Qingshan Wang<sup>1,2</sup>

Gas turbine engines of tanks, which are land-based derivatives of aero-turboshaft engines, share core gas generator rotor structures but face significantly higher external impact loads due to combat environments, require enhanced dynamic performance, especially in resisting rotor-casing rub-impact response. To address this, a dynamic model of the rotor system is established, employing the equivalent ring principle for the circular arc end-teeth connection structure, the differential quadrature finite element method (DQFEM) for variable-section blades, and the lumped parameter method for modeling the disks. The supporting system, which incorporates squeeze film dampers (SFDs), is constructed based on oil film and short bearing theory. Using Coulomb's friction law, a blade-casing rub-impact dynamic model is developed. The accuracy of the model is verified through modal testing. A parametric study is conducted to explore the influence of impact load amplitude, support damping, blade-casing stiffness and clearance, and unbalanced mass on the rub-impact response of the rotor-casing system. The proposed model and findings are applicable to both vehicle-mounted gas turbines and aero-turboshaft engine rotors. The results are useful in the design and optimization of vehicle-mounted gas turbines under high external impact loads.

**Keywords** Gas generator rotor, Circular arc end-teeth, Rub-impact, Blade-casing system, Numeric modeling

The gas generator rotor systems of turboshaft aero engines and automotive gas turbines share similar architectures, characterized by multiple support points, large spans, and multi-component rotors. In such high-speed machinery, the blade-tip clearance—the small gap between the rotor blade tips and the inner wall of the casing—is a critical parameter for overall performance and efficiency. To minimize working-fluid (e.g., gas) leakage, this clearance should theoretically be made as small as possible; however, an excessively tight clearance significantly increases the risk of blade-to-casing frictional contact, or “rubbing”. These transient rubbing events not only can cause localized damage to blades, seals, or casing, but also induce severe vibration amplification, often accompanied by seal wear, shaft thermal bowing, and abnormal noise. According to<sup>1</sup>, blade-casing rubbing is one of the most common failure modes in aircraft engines. In automotive gas turbines, the dynamic challenges imposed by multiple supports and large spans are even more pronounced. Moreover, the stringent demands of compactness and rapid transient response in vehicle applications complicate thermal deformation management and clearance control; operating under wide temperature and load ranges further amplifies rubbing risks due to intense transient shocks.

Stator-rotor rubbing is a highly complex nonlinear dynamic phenomenon, which can be divided into radial rubbing, axial rubbing and a combination of both according to the rubbing direction<sup>2</sup>. Among them, radial rubbing is more common and can be further divided into full-circle rubbing<sup>3–5</sup> and partial rubbing<sup>6–8</sup> according to the contact area. The forms of full-circle rubbing mainly include synchronous full-circle rubbing and reverse full-circle rubbing. Synchronous full-circle rubbing is a typical forced vibration, in which the eddy direction of the rotor is consistent with the rotation direction, the contact force is small, and the harmfulness is low; reverse full-circle rubbing is a self-excited vibration caused by “dry friction”, the eddy direction is opposite to the rotation direction, which will produce severe vibration and may cause serious damage to rotating machinery in a very

<sup>1</sup>College of Mechanical and Electrical Engineering, Central South University, Changsha 410083, PR China. <sup>2</sup>State Key Laboratory of Precision Manufacturing for Extreme Service Performance, Central South University, Changsha 410083, PR China. <sup>3</sup>Hunan Aviation Powerplant Research Institute, Aero Engine Corporation of China, Zhuzhou 412002, PR China. <sup>4</sup>School of Civil Engineering, Central South University, Changsha 410075, PR China. ✉email: liutaosr@csu.edu.cn

short time<sup>9</sup>. According to the contact position and area, partial rubbing can be further subdivided into single-point rubbing, multi-point rubbing, eccentric rubbing, and coupled rubbing of point and eccentric rubbing, etc.

Extensive research has explored the dynamic behavior of blade-casing rubbing in turbomachinery. Early work focused on developing dynamic models to characterize the vibrational responses of rotor systems under various rubbing conditions. For instance, Li et al.<sup>10</sup> introduced a modified rotating blade-casing model based on elastic compatibility, which more accurately predicted casing deformation and vibration responses. Similarly, Guo et al.<sup>11</sup> improved upon existing models by incorporating the flexibility of both rotating blades and the casing, leading to a more accurate analysis of the system's rub-impact response.

To enhance computational efficiency and accuracy, researchers have also explored advanced modeling techniques. Sun et al.<sup>12</sup> demonstrated that using a Variable Thickness Torsional Shell (VITS) model for blades significantly improves computational speed while maintaining accuracy. Zeng et al.<sup>13–15</sup> developed a reduced-order FEM to analyze the influence of support stiffness on frictional behavior and resonance sensitivity. Li et al.<sup>16</sup> established a dynamic model of a dual-rotor system with bolted connections in the high-pressure rotor based on the Timoshenko beam element, and the rubbing response characteristics of the low-pressure rotor and the high-pressure rotor were analyzed. Hong et al.<sup>17</sup> found that material properties and unbalanced mass significantly affect stress distribution on blades during rubbing, exacerbating stress concentration. Jin<sup>18</sup> established a dynamic model for the rotor-blade-casing system of a turboshaft engine with curvic coupling connections, and investigated the influence of pre-tightening forces on the system's natural characteristics and nonlinear rub-impact responses. These studies highlight the need for refined models that can capture the complex dynamics of blade-casing interactions.

The operational stability of gas-generator rotors in turboshaft engines is critical for helicopters and high-speed tracked vehicles that are routinely exposed to severe shock loads. Emergency landings, deck landings, gunfire and off-road travel transmit high-amplitude transients through the engine mount, markedly altering rotor dynamics and raising the probability of rotor–casing contact.

Previous research has investigated the dynamic characteristics of rotor systems under similar conditions. Duchemin et al.<sup>19</sup> and Sousa et al.<sup>20</sup> both used theoretical and experimental methods to analyze flexible rotor systems subjected to base excitation, confirming the significant influence of support motion. Further, Dakel et al.<sup>21</sup> developed a Timoshenko beam-based model that incorporated six base motions, revealing lateral dynamic instability from parametric excitations. In the context of aero-engines, Gao et al.<sup>22</sup>, Zheng et al.<sup>23</sup> and Wang et al.<sup>24</sup> established dynamic models to study the impact of maneuver loads on rotor systems, demonstrating how such overloads can lead to amplified vibrations and complex nonlinear responses. Liu et al.<sup>25</sup> also highlighted the importance of considering base motion on hydrodynamic oil-film forces, showing its significant influence on dynamic responses.

Beyond simple base excitation, researchers have delved into more complex rub-impact scenarios. Zhang et al.<sup>26</sup> studied a coupled bending-torsional system with rub-impact, finding that mass eccentricity and electromagnetic torque can induce unstable responses. Wang et al.<sup>27</sup> and Qi et al.<sup>28</sup> investigated coupled faults and multi-factor interactions in dual-rotor systems, revealing complex nonlinear behaviors like bifurcation and chaos. Lin et al.<sup>29</sup> provided a detailed analysis of high-/low-order mode coupling and parameter-driven instability in dual-rotor systems. These studies underscore the complexity of rotor dynamics when multiple factors—such as base motion, maneuver loads, and rub-impact—are at play.

Although previous work on gas-generator rotors has focused on aero-engines, aero-derivative gas turbines operate under uniquely severe conditions. Armoured-vehicle turboshafts, for example, must survive intense transients generated by artillery fire, obstacle traversal and broadband vibration; these shocks, transmitted through the engine mount, markedly increase the likelihood of rotor–casing contact. Consequently, the rub-impact behavior of such systems under high-intensity base excitation demands systematic study. While extant models, advanced diagnostic techniques and controlled experiments have improved general understanding of rub phenomena, they do not account for the distinctive geometry and extreme external loading characteristic of aero-derivative turbines.

This paper addresses this critical gap by focusing on the rub-impact response of a gas generator rotor system specifically for a tank gas turbine application. We make several key contributions, beginning with the development of a novel equivalent dynamic model for the unique circular arc end-teeth connection structure. This is followed by a comprehensive modeling approach that combines the differential quadrature finite element method (DQFEM) for variable-section blades with the lumped parameter method for rotating disks. Furthermore, we establish a complete rub-impact dynamic model tailored for external impact excitation, incorporating a support system with a squeeze film damper and the rub-impact excitation force. Finally, the model's validity is confirmed through modal experiments, and we provide a detailed analysis of the system's rub-impact response characteristics under a range of impact excitations and key structural parameters. Crucially, the model established in this paper and the results obtained are not only applicable to gas generator rotors for tanks, but can also provide certain guidance for the impact resistance design optimization of gas generator rotors for aviation turboshaft engines.

## Dynamic modeling of gas generator rotor rub-impact response under external load

### Description of the model

This paper investigates the rub-impact mechanism of a gas-generator rotor in an aero-derivative turboshaft engine subjected to external shock. When a helicopter executes a shipboard or emergency landing with an excessive sink rate (Fig. 1a), the vertical kinetic energy is converted into an impulsive load that is transmitted to the engine mount through the landing-gear–airframe path. From a rotor dynamic perspective, this sudden disturbance upsets the dynamic balance of the gas generator rotor. When the vibration amplitude exceeds the designed clearance between the rotor blades and the casing, the rotor-casing rub-impact fault is triggered.

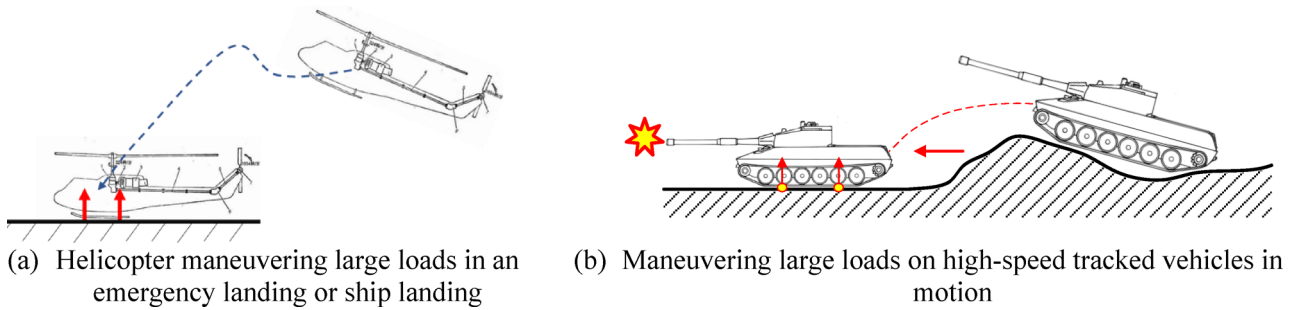


**Fig. 1.** Schematic diagram of external shock loads on the gas generator rotor system in a turboshaft engine.

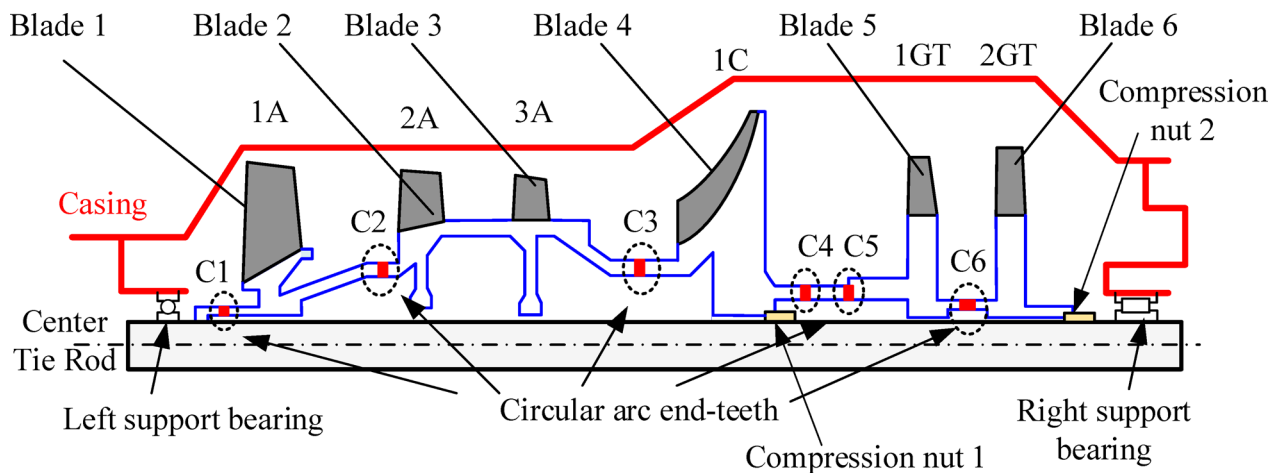


**Fig. 2.** Schematic diagram of the rotor blade-casing system for the gas generator.

Notably, vehicle gas turbines (such as AGT-1500) and aero-turboshaft engines (such as T700) exhibit significant structural similarity of gas generator rotors, both adopting the typical configuration of multi-stage axial/centrifugal compressors and gas turbines. This structural similarity means that in scenarios such as slope impacts and artillery firing of high-speed tracked vehicles, the transient loads generated when vehicle kinetic energy is converted into gravitational potential energy, as well as the pulse excitation caused by the reaction force of artillery firing, will still be transmitted to the rotor system in the form of stress waves through the engine base despite buffering by the suspension system. The excitation of high-speed tracked vehicles in scenarios such as flying slope impacts and artillery firings can also lead to a risk of rub-impact in the gas generator rotor system (Fig. 1b).

Figure 2 depicts the gas-generator rotor model analyzed in this study. The configuration is representative of contemporary turboshaft engines and is readily scalable to aeroderivative units. Major components comprise a single-stage centrifugal compressor (disk 1 C), three axial-compressor disks (1 A, 2 A, 3 A), two turbine stages (1GT, 2GT), a central tie-rod, a compression nut, left and right bearings, and an outer casing. Disk 1 A is machined from TC4 titanium alloy; disks 2 A, 3 A and the impeller are fabricated from TC11; both turbine rotors are cast from GH4720Li nickel-based superalloy.

The gas generator rotor model comprises a central tie-rod, a stacked disk-bladed-disc assembly, compression nuts, and left/right bearings. The curvic coupling is represented by an equivalent ring element; the tie-rod by uniform beam elements; disks and blades by tapered beam elements. Preload in the nuts is applied as an axial force between the centrifugal impeller and the second-stage turbine disk, while each bearing support is modelled as a parallel spring-damper pair.

### Equivalent dynamic modeling of the circular Arc end-tooth structures

For the gas generator rotor system, the circular end tooth connection structure is mainly used for the connection and centering of discontinuous rotor components by contact interface extrusion. During the manufacturing of circular arc end-tooth structures, micro-roughness inevitably exists on the contact interface due to constraints in processing methods and precision. This feature causes the actual interface contact area at the end-teeth connection of the rotor structure to be significantly smaller than the theoretical value, triggering discontinuous mutations in contact stress. These factors lead to geometric discontinuities and mass mutations in the rotor system's material distribution, as well as stiffness degradation in mechanical properties. Based on solid mechanics and interface contact mechanics theories, the stiffness loss of circular arc end-tooth structures can be expressed as:

$$K_{contact} = \eta K_{contact}^p \tag{1}$$

where  $K_{contact}$  represents the contact stiffness of the circular arc end-tooth structures, and  $K_{contact}^p$  represents the contact stiffness of the circular arc end-tooth structures under the initial axial load.  $\eta$  is the overall stiffness loss correction coefficient:

$$\eta = \eta_1 \cdot \eta_2 \cdot \eta_3 \tag{2}$$

where the  $\eta_1$ ,  $\eta_2$ , and  $\eta_3$  are the interfacial contact area coefficient, the correction factor for the interfacial contact effect and the correction factor for the stiffness resulting from the bending deformation of the circular arc end-teeth, respectively.

When the contact area of the circular arc end-teeth contacts section changes, it is generally characterized by the interface contact area coefficient  $\eta_1$ .

As shown in Fig. 3,  $A_T$  represents the equivalent projected area of any contact tooth surface on the  $x$ - $y$  plane;  $A_C$  represents the nominal contact area of any contact tooth surface of the circular arc end-tooth structure, and the specific expression is as follows:

$$A_C = \frac{(D_{out} - D_{ine}) h_f}{4 \cos \theta} Z_c \tag{3}$$

where  $D_{out}$  and  $D_{ine}$  are the outer and inner diameters of the tooth,  $h_f$  is the tooth height.  $A_{act}$  represents the actual contact area of any contact tooth surface, and the specific expression is as follows:

$$A_{act} = \sum_{i=1}^{n_{wt}} a_{wt} \tag{4}$$

in the equation,  $P_{wt}$  is the unit distribution density of asperities in microtopography, which is determined by surface roughness and statistically follows a Gaussian normal distribution function;  $n_{wt}$  represents the mathematical expectation of asperity numbers on any contact surface.

$a_{wt}$  signifies the contact area of a single asperity. According to the solid interface contact theory, it can be expressed as:

$$a_{wt} = \begin{cases} \pi R^* \omega_a, & \omega_a \leq \omega_e \\ \pi R^* (a_1 \omega_a^3 + a_2 \omega_a^2 + a_3 \omega_a + a_4), & \omega_e \omega_a \omega_p \\ 2\pi R^* \omega_a, & \omega_a \geq \omega_p \end{cases} \tag{5}$$

where  $R^*$  is the equivalent curvature radius of the asperity top;  $\omega_a$  is the normal deformation of the asperity,  $\omega_a = z_{wt} - h_{CC}$ ;  $h_{CC}$  is the distance between rough surfaces;  $E^*$  is the equivalent elastic modulus generated by the contact surface:  $E^* = [(1-\mu_1)/E_1 + (1-\mu_2)/E_2]^{-1}$ ;  $E_1$  and  $E_2$  are the elastic moduli of the two contact surfaces;  $\mu_1$  and  $\mu_2$  are the Poisson's ratios of the two contact surfaces;  $K_\mu$  denotes the average contact pressure coefficient:  $K_\mu = 0.454 + 0.41\mu_2$ ;  $\omega_e$ ,  $\omega_p$ ,  $a_1$ ,  $a_2$ ,  $a_3$  and  $a_4$  are correlation coefficients:

$$\begin{aligned} \omega_e &= \left( \frac{3\pi K_\mu H}{4E^*} \right)^2 R^*; \omega_p = 110\omega_e; a_1 = \frac{(\omega_e + \omega_p)}{(\omega_e - \omega_p)^3}; a_2 = -2(\omega_e + \omega_p) a_1 \\ a_3 &= \frac{2\omega_e^3 - 2\omega_e^2\omega_p + 7\omega_e\omega_p^2 - \omega_p^3}{(\omega_e - \omega_p)^3}; a_4 = -\frac{2\omega_e^2\omega_p^2}{(\omega_e - \omega_p)(\omega_e^2 - 2\omega_e\omega_p + \omega_p^2)} \end{aligned} \tag{6}$$

The roughness of the circular arc end-tooth contact interface can be characterized by asperities of varying heights (as shown in Fig. 4). Under the assumption of material isotropy throughout the component, contact surface asperities differ only in geometric morphology. Under external forces, deformation state variations among

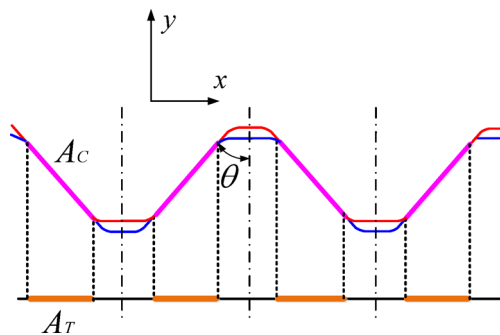


Fig. 3. Schematic diagram of the correction of contact area loss at the interface of the circular arc end-teeth.

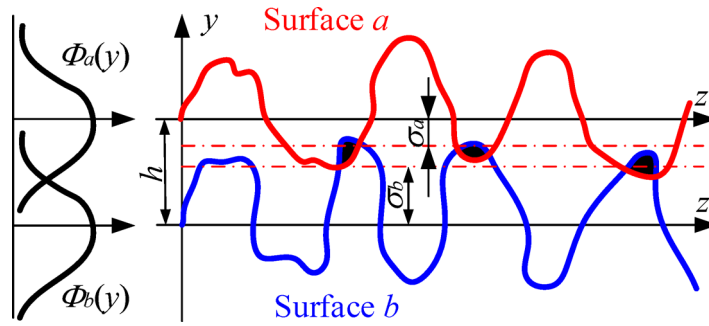


Fig. 4. Schematic diagram of contact characteristics of the rough interface of circular arc end teeth.

asperities with different morphologies result in three contact characteristics: (1) elastic contact; (2) elastoplastic contact; (3) plastic contact. For the same contact area, variations in contact characteristics lead to differences in contact stiffness, typically characterized by the interface contact effect correction coefficient  $\eta_2$ .

Based on the elastoplastic contact theory, the relationship between the interface contact force and asperity deformation is expressed as:

$$f_{wt} = \begin{cases} \frac{4}{3} E^* R^{*\frac{1}{2}} \omega_a^{\frac{3}{2}} a_{wt}, \omega_a \leq \omega_e \\ H \left[ 1 - (1 - K_\mu) \frac{\ln \omega_p - \ln \omega_a}{\ln \omega_p - \ln \omega_e} \right] a_{wt}, \omega_e \omega_a \omega_p \\ H^* a_{wt}, \omega_a \geq \omega_p \end{cases} \quad (7)$$

where  $H^*$  is the surface hardness of the softer material among the two contact surfaces. The interface stiffness  $K_2$  without considering the contact effect and the interface stiffness  $K'_2$  considering the contact effect are expressed as follows:

$$K_2 = E^* A_{act}; K'_2 = \frac{f_{wt}}{\omega} \quad (8)$$

Thus, the interface contact effect correction coefficient  $\eta_2$  can be determined:

$$\eta_2 = K'_2 / K_2 \quad (9)$$

The initial loads in the rotor system significantly affect the bending stiffness characteristics of the structure. When the structural stiffness is enhanced by applying axial preload, the introduction of additional bending moments leads to the stiffness degradation of the connected structure. Therefore, when considering the bending deformation of the preloaded combined rotor, its stiffness degradation is characterized by the rotor bending deformation correction factor  $\eta_3$ .

For the gas generator rotor system, a preload must be applied in its operating condition to ensure overall structural rigidity. At this time, the expression for the bending stiffness of the circular arc end teeth is:

$$k'_{3L} = \frac{16EI}{l_1^3} \cdot \frac{u_1^3}{\tan u_1 - u_1}; k'_{3R} = \frac{16EI}{l_2^3} \cdot \frac{u_2^3}{\tan u_2 - u_2} \quad (10)$$

$$u = \sqrt{\frac{F_p l^2}{4EI}} \quad (11)$$

where  $k'_{3L,R}$  represents the structural bending stiffness caused by the initial load;  $u_1$  and  $u_2$  respectively represent the influence of the preload on the structural bending stiffness of the left and right components. Therefore, the bending deformation correction factor  $\eta_3$  can be expressed as:

$$\eta_{3L} = 1 - \frac{1}{3} \frac{u_1^3}{\tan u_1 - u_1}; \eta_{3R} = 1 - \frac{1}{3} \frac{u_2^3}{\tan u_2 - u_2} \quad (12)$$

Up to this point, the circular arc end teeth stiffness loss model can be determined by substituting Eqs. (12), (10) and (3) back into Eq. (1). Under the consideration of stiffness degradation influencing factors, this paper adopts the equivalent ring structure to simulate the circular arc end-tooth connection structure, as shown in Fig. 5.  $b_L$  and  $b_R$  are the thickness of the left and right end-teeth,  $b_c$  denotes the thickness of the engagement region of the end-teeth. The equivalent ring is rigidly connected with the left and right end disk structures, and the strain energy and mass of the equivalent ring structure remain constant with the end-teeth connection structure.

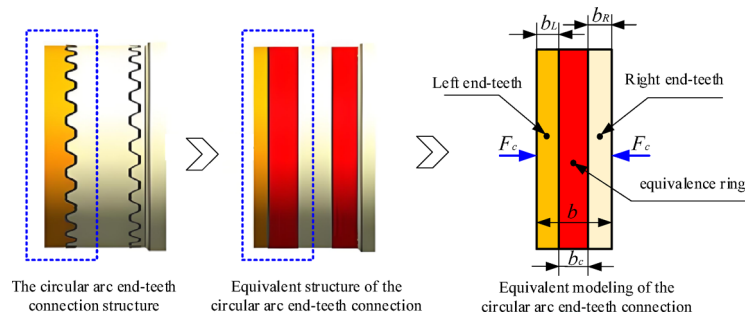


**Fig. 5.** Schematic of equivalent modeling of circular arc end teeth connection structure.

Name	Material	Elastic modulus (GPa)	Density (kg/m <sup>3</sup> )	Poisson's Ratio
C1	TC4	109	4440	0.34
C1(Equivalent ring)	--	73.80	4401.07	0.3
C2	TC4	109	4440	0.34
C2(Equivalent ring)	--	68.64	4347.21	0.3
C3	TC11	123	4480	0.33
C3(Equivalent ring)	--	72.93	4366.70	0.3
C4	GH4720Li	225	8140	0.35
C4(Equivalent ring)	--	155.76	6130.61	0.3
C5	GH4720Li	225	8140	0.35
C5(Equivalent ring)	--	220.38	7906.39	0.3
C6	GH4720Li	225	8140	0.35
C6(Equivalent ring)	--	211.66	7886.85	0.3

**Table 1.** Material properties of six end-teeth connect structures and the equivalent model.

Drawing from our previous work<sup>30</sup>, the elastic modulus, density, and Poisson's ratio of the equivalent ring structure, subject to a normal preload force  $F_c$ , are determined as follows:

$$E_{equ} = \frac{K_{contact} E_L E_R (b_L + b_R)}{K_{contact} b_L E_R + K_{contact} b_R E_L + A_c E_L E_R} \tag{13}$$

$$\rho_{equ} = \frac{\rho_L \cdot V_L + \rho_R \cdot V_R}{V_L + V_R} \tag{14}$$

$$\mu_{equ} = \frac{\left[ \frac{\mu_L F_c b_L}{E_L A_c} + \frac{\mu_R F_c b_R}{E_R A_c} + \frac{F_c (\mu_L + \mu_R)}{2 K_{contact}} \right] E_{equ} A_c}{F_c (b_L + b_R)} \tag{15}$$

where  $E_L$  and  $E_R$  denote the elastic modulus of the left and right end teeth, respectively;  $A_c$  denotes the contact area of the end-teeth.

As illustrated in Fig. 2, the gas generator rotor system under investigation incorporates six circular arc end-tooth connection structures. The equivalent ring modeling method, predicated on virtual material layering, was employed to represent these six structures. Material parameters, both prior to and following this equivalent representation, are detailed in Table 1.

### Modeling of rotating disk-blade system

To model the dynamic behavior of the gas generator rotor system shown in Fig. 2, a simplified disk-blade system is established. As in our previous work<sup>30</sup>, the specific modeling and derivation processes are omitted here; this section provides the final energy expressions.

The system's components are modeled as a hollow rigid disk and variable cross-section blades. The dynamic model for the rigid disk is based on the centralized parameter method (Fig. 6), with its kinetic energy expression given by:

$$T_{disk} = \frac{1}{2} M_d (\dot{X}_c^2 + \dot{Y}_c^2 + \dot{Z}_c^2) + \frac{1}{2} J_d (\dot{\theta}_X^2 + \dot{\theta}_Y^2) + \frac{1}{2} J_p (\Omega + \psi) [\Omega + \psi - 2\dot{\theta}_Y \theta_X] \tag{16}$$

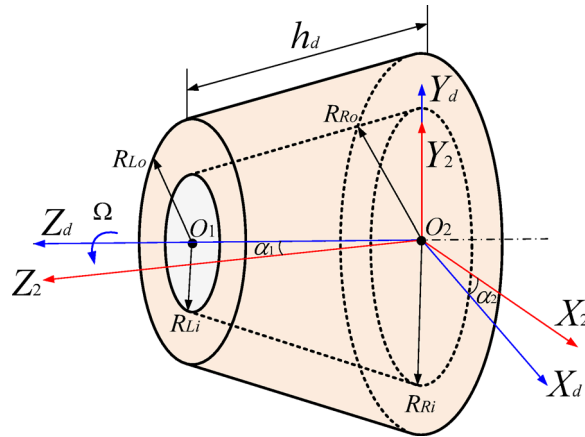


Fig. 6. Schematic diagram of the hollow rigid disk.

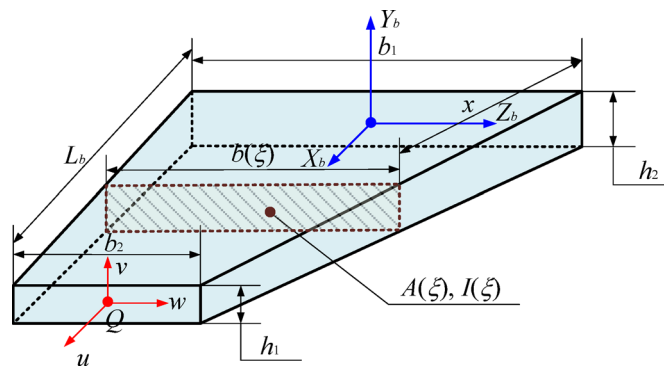


Fig. 7. Schematic diagram of the variable cross-section blade.

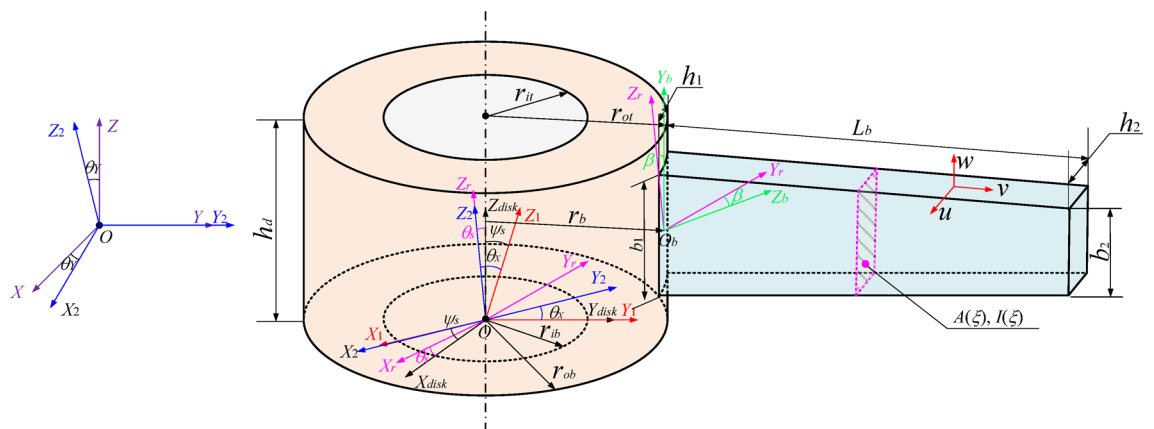


Fig. 8. Schematic diagram of the disk-blade coupling system.

where  $X_c, Y_c$  and  $Z_c$  are the displacements along the  $X_d, Y_d$  and  $Z_d$  directions, respectively.

Similarly, the variable cross-section blades are mounted on the disk assembly (Figs. 7 and 8). The kinetic and potential energy expressions for the  $i$ -th rotating blade, considering bending, axial compression, shear, and centrifugal forces, are as follows:

$$T_{blade} = \frac{1}{2} \rho_b \int_0^{L_b} A(x) \dot{\mathbf{r}}_Q^2 dx = \frac{1}{2} (T_1 + T_2 + T_3) \tag{17}$$

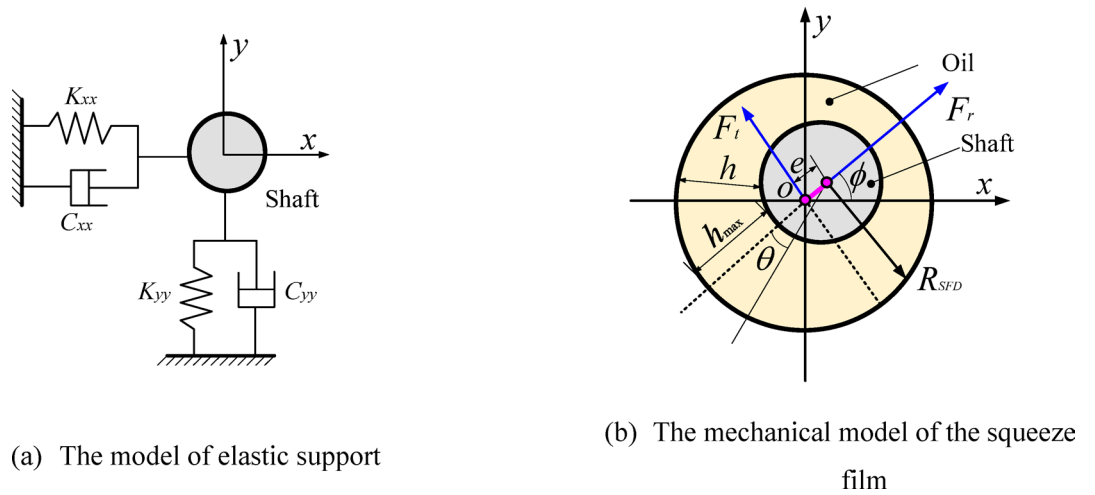


Fig. 9. Model of the SFD support system.

$$\begin{aligned}
 \mathbf{U}_{blade} = & \frac{1}{2} \int_0^{L_b} f_c(x) \left( \frac{\partial v}{\partial x} \right)^2 dx + \frac{1}{2} \int_0^{L_b} E_b I(x) \left( \frac{\partial \varphi}{\partial x} \right)^2 dx \\
 & + \frac{1}{2} \int_0^{L_b} E_b A(x) \left( \frac{\partial u}{\partial x} \right)^2 dx + \frac{1}{2} \int_0^{L_b} \kappa_b A(x) G_b \left( \frac{\partial v}{\partial x} - \varphi \right)^2 dx
 \end{aligned} \tag{18}$$

where  $E_b$ ,  $G_b$ , and  $\kappa_b$  are the elastic modulus, shear modulus, and shear factor of the blade, respectively;  $f_c$  denotes the centrifugal force of the rotating blade:

$$\mathbf{f}_c(x) = \int_x^{L_b} df_c(x) = \rho_b \Omega^2 \int_x^{L_b} A(x)(r_b + x) dx \tag{19}$$

According to the above derivation, the energy expression of the disk-blade system can be obtained as follows:

$$\begin{aligned}
 T_{blade-disk} &= T_{disk} + \sum_{i=1}^{N_b} T_{blade}^i \\
 U_{blade-disk} &= \sum_{i=1}^{N_b} U_{blade}^i
 \end{aligned} \tag{20}$$

### Modeling of support systems with squeezed film dampers

Squeeze Film Dampers (SFDs) are widely applied in the support systems of aero-engine gas generator rotors due to their simple structure, excellent vibration damping performance, and high reliability. The gas generator rotor system of a turboshaft engine typically adopts a 1-0-1 support scheme, as shown in Fig. 2. Engineering practice indicates that when the rotor system is subjected to maneuvering large-load impacts, the damping of the support structure can effectively dissipate rub-impact energy and suppress local rub-impact. The support stiffness is also crucial for the rotor’s motion state after impact. A reasonable design of the support system can ensure the operational stability of the rotor system under large loads and avoid damage to the support structure. For simplification, based on model mechanism analysis, this paper uses an elastic support model composed of parallel spring-damper elements to equivalently simulate the support system with SFD, and establishes its dynamic model (Fig. 9), where Fig. 9(a) represents the elastic support model and Fig. 9(b) represents the squeeze film mechanical model.

To condense the paper, the expressions for the support stiffness  $K_{SFD}$  and damping  $C_{SFD}$  are provided below. The relevant derivation process can be found in our previous work<sup>30</sup>.

$$K_{SFD} = \frac{2\mu_{SFD} R_{SFD} L_{SFD}^3 \varepsilon_{SFD} \dot{\phi}}{C_{SFD}^3 (1 - \varepsilon_{SFD}^2)^2}; C_{SFD} = \frac{\pi \mu_{SFD} R_{SFD} L_{SFD}^3}{2C_{SFD}^3 (1 - \varepsilon_{SFD}^2)^{1.5}} \tag{21}$$

### Dynamic modeling of the blade-casing system

During the operation of the gas generator rotor system, significant vibrations occur in the rotor due to maneuvering impact loads, leading to rub-impact between the blades and the casing. When rub-impact happens, interactive forces are generated between the blades and the casing. To analyze the influence of these interactive forces, this section establishes a blade-casing rub-impact model as shown in Fig. 10. The model simplifies the casing as a stationary, rigid body, and solves for the rub-impact forces between the blades and the casing based

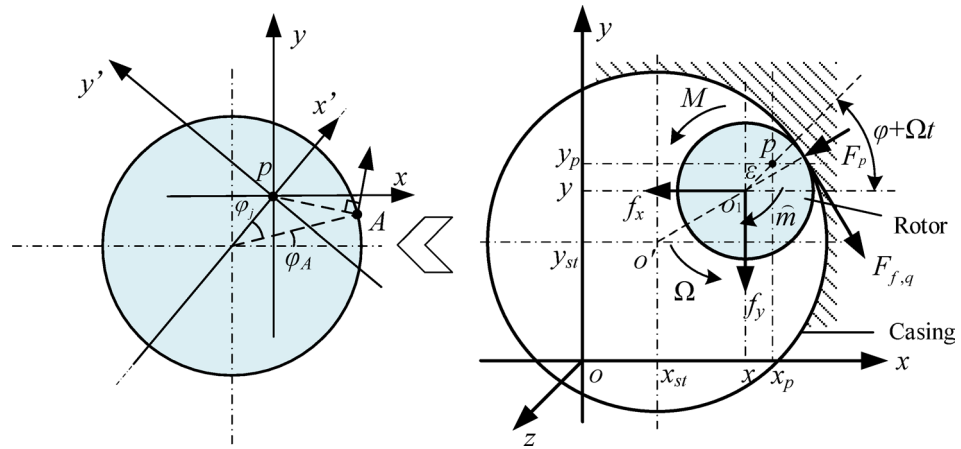


**Fig. 10.** The contact force analysis model for blade-casing systems.

on previous studies. For this specific application, where the rotor system is subjected to high external impact loads and the casing is significantly stiffer and heavier than the flexible blades, simplifying the casing as a rigid body is a reasonable approximation. This assumption allows for a focus on the primary dynamic response of the rotor and blades without the added complexity of casing deformation. Under normal operating conditions, a designed clearance is maintained between the blades and the casing. When this clearance diminishes to zero, rub-impact occurs, exerting two main types of forces on the blades: a normal impact force and a tangential friction force.

(1) Normal Impact Force.

As shown in Fig. 10, the normal impact force refers to the normal force at the collision point, with the specific expression as:

$$F_p = K_p \cdot \delta_p^{3/2} + K_p \cdot \delta_p^{3/2} \frac{3}{2} \alpha_C \dot{\delta}_p \tag{22}$$

in the equation,  $K_p$  denotes the equivalent rub-impact stiffness between the blade and the casing, specifically expressed as:  $K_p = k_b k_c / (k_b + k_c)$ ;  $k_b$  and  $k_c$  represent the radial equivalent stiffness of the blade and the casing, respectively;  $\alpha_C$  is the energy consumption constant, with a value of 0.16s/m;  $\delta_p$  indicates the rub-impact deformation, and its specific expression is:

$$\delta_p = \sqrt{[x_p + r \cos \varphi_A - \varepsilon \cos(\varphi + \Omega t) - x_{st}]^2 + [y_p + r \sin \varphi_A - \varepsilon \sin(\varphi + \Omega t) - y_{st}]^2 - r_{rot} - c_{sr}} \tag{23}$$

where  $r_{rot}$  represents the rotor radius, i.e., the distance from the blade tip to the axis;  $c_{sr}$  is the gap between the blade and the casing. The rate of change of the rub-impact deformation can be decomposed into the normal velocity of the blade tip rub-impact point A relative to the disk centroid p and the normal velocity of the disk centroid p relative to the casing, with the specific expression as:

$$\begin{aligned} \dot{\delta}_p &= v_x^A \cos \varphi_A + v_y^A \sin \varphi_A + (\dot{x}_p - \dot{x}_{st}) \cos \varphi_A + (\dot{y}_p - \dot{y}_{st}) \sin \varphi_A \\ &= [\dot{x}_p - \dot{x}_{st} + \varepsilon(\Omega + \dot{\varphi}) \sin(\varphi + \Omega t)] \cos \varphi_A \\ &\quad + [\dot{y}_p - \dot{y}_{st} - \varepsilon(\Omega + \dot{\varphi}) \cos(\varphi + \Omega t)] \sin \varphi_A \end{aligned} \tag{24}$$

(2) Frictional Force.

According to Coulomb's friction theorem, the frictional force between the blade and the casing can be regarded as two frictional components at the rub-impact point A on the tangent plane (perpendicular to the normal direction) of the casing at the moment of rub-impact, with the specific expression as:

$$\begin{cases} F_{f,z} = -v_z^{A,j} / \sqrt{(v_z^{A,j})^2 + (v_q^{A,j})^2} \cdot \mu |F_p| \\ F_{f,q} = -v_q^{A,j} / \sqrt{(v_z^{A,j})^2 + (v_q^{A,j})^2} \cdot \mu |F_p| \end{cases} \tag{25}$$

in which  $\mu$  represents the rub-impact friction coefficient, the expressions of the velocity components  $v_z^{A,j}$  and  $v_q^{A,j}$  are as follows:

$$\begin{aligned}
 v_z^{A,j} &= v_z^A = r\dot{\varphi}_{x_1} \sin \varphi_A - r\dot{\varphi}_y \cos \varphi_A + r(\Omega + \dot{\varphi})(\varphi_{x_1} \cos \varphi_j - \varphi_y \sin \varphi_j) \\
 v_q^{A,j} &= -v_x^A \sin \varphi_A + v_y^A \cos \varphi_A - (\dot{x}_p - \dot{x}_{st}) \sin \varphi_A + (\dot{y}_p - \dot{y}_{st}) \cos \varphi_A \\
 &= r(\Omega + \dot{\varphi}) - [\dot{x}_p - \dot{x}_{st} + \varepsilon(\Omega + \dot{\varphi}) \sin(\varphi + \Omega t)] \sin \varphi_A \\
 &\quad + [\dot{y}_p - \dot{y}_{st} - \varepsilon(\Omega + \dot{\varphi}) \cos(\varphi + \Omega t)] \cos \varphi_A
 \end{aligned}
 \tag{26}$$

By synthesizing and decomposing the rub-impact excitation forces obtained from the above analysis, the components of the rub-impact excitation force between a single blade and the casing in the  $x$  and  $y$  directions are obtained, and the expressions of the rub-impact excitation force components are as follows:

$$\begin{cases} F_x^* = -|F_p| \cdot \cos \varphi_A - F_{f,q} \cdot \sin \varphi_A \\ F_y^* = -|F_p| \cdot \sin \varphi_A + F_{f,q} \cdot \cos \varphi_A \end{cases}
 \tag{27}$$

Summing the rub-impact excitation forces generated by all blades, the force of rub-impact on the entire rotor system can be obtained, specifically as:

$$F_x = \sum_{k=1}^{n_{blade}} F_x^k; F_y = \sum_{k=1}^{n_{blade}} F_y^k
 \tag{28}$$

When rub-impact occurs between the blade and the casing, the work done by the rub-impact frictional force is  $W_{rub}$ , with the specific expression as:

$$W_{rub} = \frac{1}{2} F_p u_L + \frac{1}{2} F_{f,q} u_L
 \tag{29}$$

Based on Hamilton's principle, the specific expressions of the kinetic energy, potential energy, and external work caused by rub-impact forces of the blade-casing system are as follows:

$$\delta \int_{t_1}^{t_2} (T_{blade} + T_{casing} - U_{blade} - U_{casing} + W_{rub}) dt = 0
 \tag{30}$$

in the equation,  $T_{casing}$  and  $U_{casing}$  represent the kinetic energy and potential energy of the casing, respectively;  $\delta$  denotes the variation symbol;  $t_1$  and  $t_2$  are time variables.

On the basis of the above derivation, the Differential Quadrature Finite Element Method (DQFEM) is used to discretize the displacement components of the rotating blade, with the specific expression as:

$$\mathbf{q} = \mathbf{l}\bar{\mathbf{q}}; \mathbf{q} = [ u(x, t) \quad v(x, t) \quad \varphi(x, t) ]^T; \bar{\mathbf{q}} = \begin{bmatrix} u(x_1, t) & v(x_1, t) & \varphi(x_1, t) \\ u(x_i, t) & v(x_i, t) & \varphi(x_i, t) \\ \vdots & \vdots & \vdots \\ u(x_N, t) & v(x_N, t) & \varphi(x_N, t) \end{bmatrix}
 \tag{31}$$

where  $\mathbf{q}$  represents the displacement column vector composed of displacement components;  $\mathbf{l}$  is the partial differential operator matrix composed of Lagrange interpolation polynomials;  $\bar{\mathbf{q}}$  denotes the discrete displacement component matrix composed of the function values of Gauss-Lobatto quadrature nodes. To intuitively illustrate the expression of the partial differential operator matrix, taking the displacement component  $\mathbf{u}$  as an example, this paper gives the discrete process of the derivative and integral operations of the displacement component:

$$\begin{aligned}
 \frac{\partial u(x, t)}{\partial x} &= \mathbf{A}_{01}^{(1)} \bar{\mathbf{u}}; \int_{-1}^1 u(x, t) dx = \mathbf{C}_{01} \bar{\mathbf{u}} \\
 \bar{\mathbf{u}} &= [ u(x_1, t) \quad u(x_i, t) \quad \cdots \quad u(x_N, t) ]^T
 \end{aligned}
 \tag{32}$$

in the equation,  $\mathbf{A}_{01}^{(1)}$  and  $\mathbf{C}_{01}$  represent the one-dimensional differential weighting coefficient matrix and integral weighting coefficient matrix, respectively, with the specific expressions as:

$$\mathbf{A}_{01}^{(1)} = \begin{bmatrix} A_{11}^{(1)} & A_{12}^{(1)} & \cdots & A_{1N}^{(1)} \\ A_{21}^{(1)} & A_{22}^{(1)} & \cdots & A_{2N}^{(1)} \\ \cdots & \cdots & \ddots & \cdots \\ A_{N1}^{(1)} & A_{N2}^{(1)} & \cdots & A_{NN}^{(1)} \end{bmatrix}; \mathbf{C}_{01} = \text{diag}(C_1, C_2, \cdots, C_N)
 \tag{33}$$

where  $A_{ij}^{(1)}$  and  $C_j$  represent the differential weighting coefficient and integral weighting coefficient, respectively, and the specific expressions can be found in Reference<sup>31</sup>.

Through variable substitution, the characteristic equation of the blade-casing system can be further obtained, with the specific expression as:

$$\begin{cases} M_{blade}\ddot{q}_{blade} + (C_{blade} + G_{blade})\dot{q}_{blade} + K_{blade}q_{blade} = F_{blade} + F_e \\ M_{casing}\ddot{q}_{casing} + C_{casing}\dot{q}_{casing} + K_{casing}q_{casing} = F_{casing} - F_e \end{cases} \quad (34)$$

in which,  $M_{blade}$ ,  $C_{blade}$ ,  $G_{blade}$ ,  $q_{blade}$  and  $F_{blade}$  represent the structure matrices and column vectors related to the variable cross-section blade;  $M_{casing}$ ,  $C_{casing}$ ,  $K_{casing}$ ,  $q_{casing}$  and  $F_{casing}$  represent the structure matrices and column vectors related to the casing;  $F_e$  is the rub-impact force between the blade and the casing;  $C_{blade}$  and  $C_{casing}$  can be determined by the Rayleigh damping matrix, with the specific expression as:

$$C_{blade,casing} = \alpha M_{blade,casing} + \beta K_{blade,casing} \quad (35)$$

in the equation,  $\alpha$  and  $\beta$  are proportional constants, with the specific expressions as:

$$\alpha = \frac{4\pi f_{n1}f_{n2}(\xi_1 f_{n2} - \xi_2 f_{n1})}{(f_{n2}^2 - f_{n1}^2)}; \beta = \frac{\xi_2 f_{n2} - \xi_1 f_{n1}}{\pi(f_{n2}^2 - f_{n1}^2)} \quad (36)$$

$$f_{n1} = f_{blade,casing}^1; f_{n2} = f_{blade,casing}^2$$

where  $\xi_1$  and  $\xi_2$  are modal damping ratios, is usually determined using frequency response experiments, and in this paper, the value is taken as  $\xi_1 = 0.01$ ,  $\xi_2 = 0.02$  because they fall within the commonly adopted engineering range for aero-engine rotor systems, which typically exhibit low damping (0.5%–2%);  $f_{blade}^1$  and  $f_{blade}^2$  are the 1st and 2nd natural frequencies of the blade, respectively;  $f_{casing}^1$  and  $f_{casing}^2$  are the 1st and 2nd natural frequencies of the casing, respectively.

### Dynamic modeling of rub-impact in gas generator rotor systems

In summary, the previous section developed dynamic models for the arc-end tooth connection structure under bending deformation, the variable cross-section blade, the disk, the support system incorporating a squeeze film damper, and the blade-casing rub-impact system. Building upon these models, this section establishes a rub-impact dynamic model for the gas generator rotor system. Key components within this system include the central tie rod, disk, variable cross-section blade, arc-end tooth connection structure, casing, and the support system with a squeeze film damper. The rub-impact dynamic model of the gas generator rotor system exhibits coupling relationships among its key components. Four representative substructure coupling systems are incorporated within the model: the rotor-support system, the disk-blade system, the rotor-arc tooth system, and the blade-casing system. The rotor-support system comprises the central tie rod, disk, and support system with a squeeze film damper, with the tie rod and disk connected by bolts, and the disk elastically connected to the support system. The disk-blade system couples the disk with the blade roots of the variable cross-section blades via co-nodes. The rotor-circular arc end-tooth system realizes coupling between disk components through the arc-end tooth connection structure. Finally, the blade-casing system couples the blade tips to the casing through rub-impact.

To further illustrate the coupling relationships of each coupling system in the rub-impact dynamic model of the gas generator rotor system, this section gives the matrix assembly diagrams of each coupling system, as shown in Fig. 11. For the rotor-support coupling system, the expression of the discretized motion differential equation is as follows:

$$M_{RRS}\ddot{q}_{RRS} + (C_{RRS} + G_{RRS})\dot{q}_{RRS} + K_{RRS}q_{RRS} = F_{RRS}$$

$$M_{RRS} = \begin{bmatrix} M_{rotor} & 0 & 0 \\ 0 & M_{rod} & 0 \\ 0 & 0 & M_{support} \end{bmatrix}; G_{RRS} = \begin{bmatrix} G_{rotor} & G_{rotor-rod} & 0 \\ -G_{rotor-rod}^{cT} & G_{rod} & 0 \\ 0 & 0 & 0 \end{bmatrix} \quad (37)$$

$$K_{RRS} = \begin{bmatrix} K_{rotor} & K_{rotor-rod}^c & K_{rotor-support}^c \\ K_{rotor-rod}^{cT} & K_{rod} & 0 \\ K_{rotor-support}^{cT} & 0 & K_{support} \end{bmatrix}; C_{RRS} = \alpha M_{RRS} + \beta K_{RRS}$$

$$F_{RRS} = [ F_{rotor} \quad F_{rod} \quad F_{support} ]^T; q_{RRS} = [ q_{rotor} \quad q_{rod} \quad q_{support} ]^T$$

in which,  $M_{RRS}$ ,  $C_{RRS}$ ,  $G_{RRS}$  and  $K_{RRS}$  represent the structure matrices related to the rotor-support coupling system;  $q_{RRS}$  and  $F_{RRS}$  represent the displacement column vector and external load column vector of the rotor-support coupling system, respectively;  $M_{rotor}$ ,  $G_{rotor}$  and  $K_{rotor}$  represent the mass matrix, gyro matrix, and stiffness matrix of the disk, respectively;  $M_{rod}$ ,  $G_{rod}$  and  $K_{rod}$  represent the mass matrix, gyro matrix, and stiffness matrix of the tie rod rotor;  $M_{support}$  and  $K_{support}$  represent the mass matrix and stiffness matrix of the support system with a squeeze film damper;  $q_{rotor,rod,support}$  and  $F_{rotor,rod,support}$  represent the displacement column vectors and external load column vectors of each component in the rotor-support coupling system;  $G_i^c$  and  $K_i^c$  denote the coupling terms.

For the disk-blade coupling system, the expression of the discretized motion differential equation of the system is as follows:

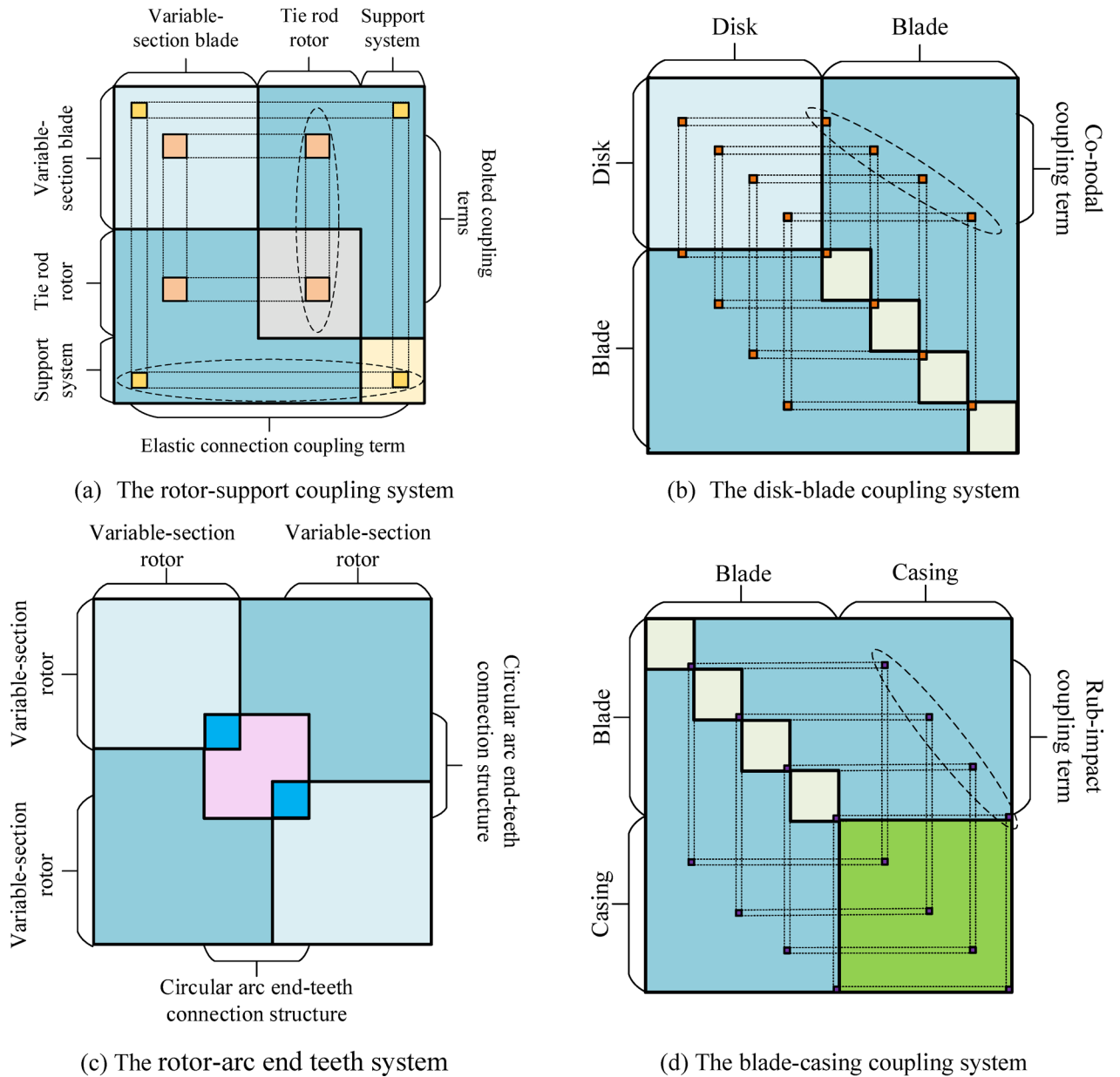


**Fig. 11.** Schematic diagram of matrix assembly for the coupling systems in the rub-impact dynamic model of the gas generator rotor system.

$$\begin{aligned}
 &M_{RB}\ddot{\mathbf{q}}_{RB} + (\mathbf{C}_{RB} + \mathbf{G}_{RB})\dot{\mathbf{q}}_{RB} + \mathbf{K}_{RB}\mathbf{q}_{RB} = \mathbf{F}_{RB} \\
 &M_{RB} = \begin{bmatrix} \mathbf{M}_{rotor} & 0 \\ 0 & \mathbf{M}_{blade} \end{bmatrix}; \mathbf{G}_{RB} = \begin{bmatrix} \mathbf{G}_{rotor} & \mathbf{G}_{rotor-blade}^c \\ -\mathbf{G}_{rotor-blade}^{cT} & \mathbf{G}_{blade} \end{bmatrix} \\
 &\mathbf{K}_{RB} = \begin{bmatrix} \mathbf{K}_{rotor} & \mathbf{K}_{rotor-blade}^c \\ \mathbf{K}_{rotor-blade}^{cT} & \mathbf{K}_{blade} \end{bmatrix}; \mathbf{C}_{RB} = \alpha\mathbf{M}_{RB} + \beta\mathbf{K}_{RB} \\
 &\mathbf{F}_{RB} = [\mathbf{F}_{rotor} \quad \mathbf{F}_{blade}]^T; \mathbf{q}_{RB} = [\mathbf{q}_{rotor} \quad \mathbf{q}_{blade}]^T
 \end{aligned} \tag{38}$$

where  $M_{RB}$ ,  $C_{RB}$ ,  $G_{RB}$  and  $K_{RB}$  represent the mass matrix, damping matrix, gyro matrix, and stiffness matrix of the disk-blade coupling system, respectively;  $q_{RB}$  and  $F_{RB}$  represent the displacement column vector and external load column vector of the disk-blade coupling system, respectively.

For the rotor-circular arc end-tooth coupling system, the expression of the discretized motion differential equation is as follows:

$$\begin{aligned}
 & \mathbf{M}_{RCR} \ddot{\mathbf{q}}_{RCR} + (\mathbf{C}_{RCR} + \mathbf{G}_{RCR}) \dot{\mathbf{q}}_{RCR} + \mathbf{K}_{RCR} \mathbf{q}_{RCR} = \mathbf{F}_{RCR} \\
 & \mathbf{M}_{RCR} = \begin{bmatrix} \mathbf{M}_{rotor} & 0 & 0 \\ 0 & \mathbf{M}_{tooth} & 0 \\ 0 & 0 & \mathbf{M}_{rotor} \end{bmatrix} \\
 & \mathbf{G}_{RCR} = \begin{bmatrix} \mathbf{G}_{rotor} & \mathbf{G}_{rotor-tooth}^c & 0 \\ -\mathbf{G}_{rotor-tooth}^{cT} & \mathbf{G}_{tooth} & \mathbf{G}_{tooth-rotor}^c \\ 0 & -\mathbf{G}_{tooth-rotor}^{cT} & \mathbf{G}_{rotor} \end{bmatrix} \\
 & \mathbf{K}_{RCR} = \begin{bmatrix} \mathbf{K}_{rotor} & \mathbf{K}_{rotor-tooth}^c & 0 \\ \mathbf{K}_{rotor-tooth}^{cT} & \mathbf{K}_{tooth} & \mathbf{K}_{tooth-rotor}^c \\ 0 & \mathbf{K}_{tooth-rotor}^{cT} & \mathbf{K}_{rotor} \end{bmatrix}; \mathbf{C}_{RCR} = \alpha \mathbf{M}_{RCR} + \beta \mathbf{K}_{RCR} \\
 & \mathbf{F}_{RB} = [ \mathbf{F}_{rotor} \quad \mathbf{F}_{tooth} \quad \mathbf{F}_{rotor} ]^T; \mathbf{q}_{RRB} = [ \mathbf{q}_{rotor} \quad \mathbf{q}_{tooth} \quad \mathbf{q}_{rotor} ]^T
 \end{aligned} \tag{39}$$

in the equation,  $\mathbf{M}_{RCR}$ ,  $\mathbf{C}_{RCR}$ ,  $\mathbf{G}_{RCR}$  and  $\mathbf{K}_{RCR}$  represent the mass matrix, damping matrix, gyro matrix, and stiffness matrix of the rotor-arc tooth coupling system, respectively;  $\mathbf{q}_{RCR}$  and  $\mathbf{F}_{RCR}$  represent the displacement column vector and external load column vector of the coupling system;  $\mathbf{M}_{tooth}$ ,  $\mathbf{G}_{tooth}$  and  $\mathbf{K}_{tooth}$  represent the mass matrix, gyro matrix, and stiffness matrix of the circular arc end-teeth connection structure;  $\mathbf{q}_{tooth}$  and  $\mathbf{F}_{tooth}$  represent the displacement column vector and external load column vector of the circular arc end-teeth connection structure, respectively.

For the blade-casing coupling system, the discretized motion differential equation of the blade-casing coupling system is shown in Eq. 34. On the basis of the above sub-system matrix assembly, the overall matrix assembly process of the rub-impact dynamic model of the gas generator rotor system is shown in Fig. 12, and the expression of the discretized motion differential equation is as follows:

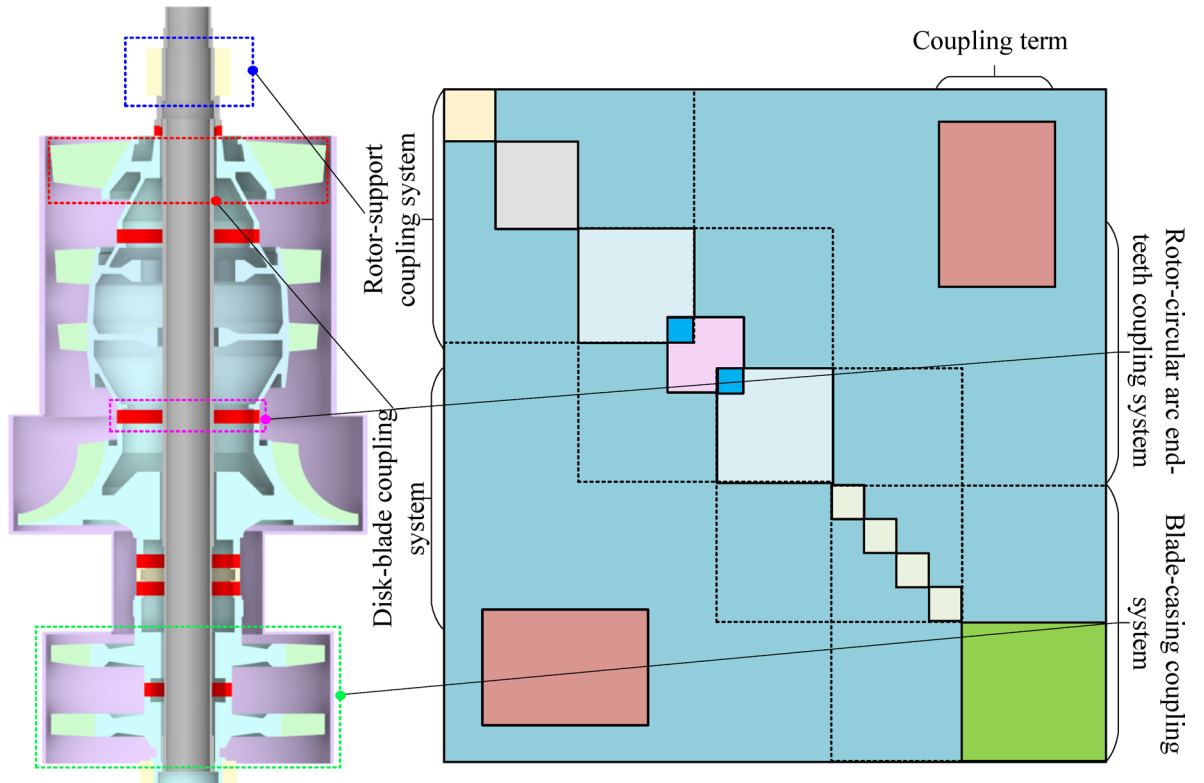


**Fig. 12.** Schematic diagram of overall matrix assembly for the rub-impact dynamic model of the gas generator rotor system.

$$\begin{cases} M_{RCSB} \ddot{\mathbf{q}}_{RCSB} + (\mathbf{C}_{RCSB} + \mathbf{G}_{RCSB}) \dot{\mathbf{q}}_{RCSB} + \mathbf{K}_{RCSB} \mathbf{q}_{RCSB} = \mathbf{F}_{RCSB} + \mathbf{F}_e \\ M_{casing} \ddot{\mathbf{q}}_{casing} + \mathbf{C}_{casing} \dot{\mathbf{q}}_{casing} + \mathbf{K}_{casing} \mathbf{q}_{casing} = \mathbf{F}_{casing} - \mathbf{F}_e \end{cases}$$

$$M_{RCSB} = \begin{bmatrix} M_{RRS} & 0 & 0 \\ 0 & M_{RCR} & 0 \\ 0 & 0 & M_{RB} \end{bmatrix}; \mathbf{G}_{RCSB} = \begin{bmatrix} \mathbf{G}_{RRS} & \mathbf{G}_{RRS-RCR}^c & \mathbf{G}_{RRS-RB}^c \\ -\mathbf{G}_{RRS-RCR}^{cT} & \mathbf{G}_{RCR} & \mathbf{G}_{RCR-RB}^c \\ -\mathbf{G}_{RRS-RB}^{cT} & -\mathbf{G}_{RCR-RB}^{cT} & \mathbf{G}_{RB} \end{bmatrix} \quad (40)$$

$$\mathbf{K}_{RCSB} = \begin{bmatrix} \mathbf{K}_{RRS} & \mathbf{K}_{RRS-RCR}^c & \mathbf{K}_{RRS-RB}^c \\ \mathbf{K}_{RRS-RCR}^{cT} & \mathbf{K}_{RCR} & \mathbf{K}_{RCR-RB}^c \\ \mathbf{K}_{RRS-RB}^{cT} & \mathbf{K}_{RCR-RB}^{cT} & \mathbf{K}_{RB} \end{bmatrix}; \mathbf{C}_{RCSB} = \alpha \mathbf{M}_{RCSB} + \beta \mathbf{K}_{RCSB}$$

$$\mathbf{F}_{RCSB} = [ \mathbf{F}_{RRS} \quad \mathbf{F}_{RCR} \quad \mathbf{F}_{RB} ]^T; \mathbf{q}_{RCSB} = [ \mathbf{q}_{RRS} \quad \mathbf{q}_{RCR} \quad \mathbf{q}_{RB} ]^T$$

where,  $M_{RCSB}$ ,  $C_{RCSB}$ ,  $G_{RCSB}$  and  $K_{RCSB}$  represent the mass matrix, damping matrix, gyro matrix, and stiffness matrix of the gas generator rotor system;  $q_{RCSB}$  and  $F_{RCSB}$  represent the displacement column vector and external load column vector of the gas generator rotor system.

### Solving procedure of rub-impact response in gas generator rotors under impact excitation

As shown in Fig. 1, helicopters and tracked vehicles experience impact loads during operation. According to Newton’s third law, the external impact force is transmitted to the engine compartment in the form of lateral forces, ultimately impacting the gas generator rotor system. Figure 13 illustrates the blade-casing contact phenomenon in the gas generator rotor under impact excitation. Under the influence of external impact excitation, the chassis imparts a fundamental excitation to the engine’s support structure. Relative motion occurs between the support structure and the rotor structure. The impact load is transmitted through the support structure to the rotor structure, inducing blade-casing contact during the process. At this point, both left and right supports simultaneously apply external dynamic impact excitations,  $F_l(t)$  and  $F_r(t)$ .

To address the external impact load excitation experienced by the gas generator rotor system during operation, this paper applies the impact acceleration in the  $y$ -direction to the left and right support structures of the gas generator rotor. Based on Newton’s second law, the work done by the impact excitation on the support nodes is:

$$\mathbf{F}_{RCSB} = \frac{1}{2} F_l \delta(u_l) + \frac{1}{2} F_r \delta(u_r) = \frac{1}{2} M_{RCSB} A_s \mathbf{u}_l + \frac{1}{2} M_{RCSB} A_s \mathbf{u}_r \quad (41)$$

In which,  $A_s$  represents the amplitude of shock acceleration;  $\mathbf{u}_l$  and  $\mathbf{u}_r$  are the position vectors of left and right support nodes. The impact excitation in this paper is modeled using a sawtooth pulse with a sharp peak, the waveform of which is shown in Fig. 14. The pulse duration ( $T_D$ ) and the peak value of the impact load are determined based on the different forms of impact loads considered.

Figure 15 illustrates the rub-impact mechanical process between a single blade and the casing, considering the structural characteristics of the gas generator rotor system. When the impact excitation is not applied, rub-impact does not occur between the rotor and the casing. The rotor undergoes synchronous forward whirling under the action of unbalanced excitation, and there is a certain clearance between the blade and the casing. When the engine is subjected to impact excitation, due to the different mass inertias of the rotor and the casing, the rotor undergoes a large vertical displacement relative to the casing, leading to the reduction of the clearance between the blade and the casing and the generation of contact, thus initiating rub-impact (as shown in Fig. 15(b)). With the occurrence of rub-impact, rub-impact loads are generated at the contact point, including normal force and tangential force. After the contact intensifies, the rub-impact force continues to increase until the maximum contact state is reached, at which time both the blade and the casing undergo significant deformation (as shown in Fig. 15(c)). When the rotor continues to move, the contact between the blade and

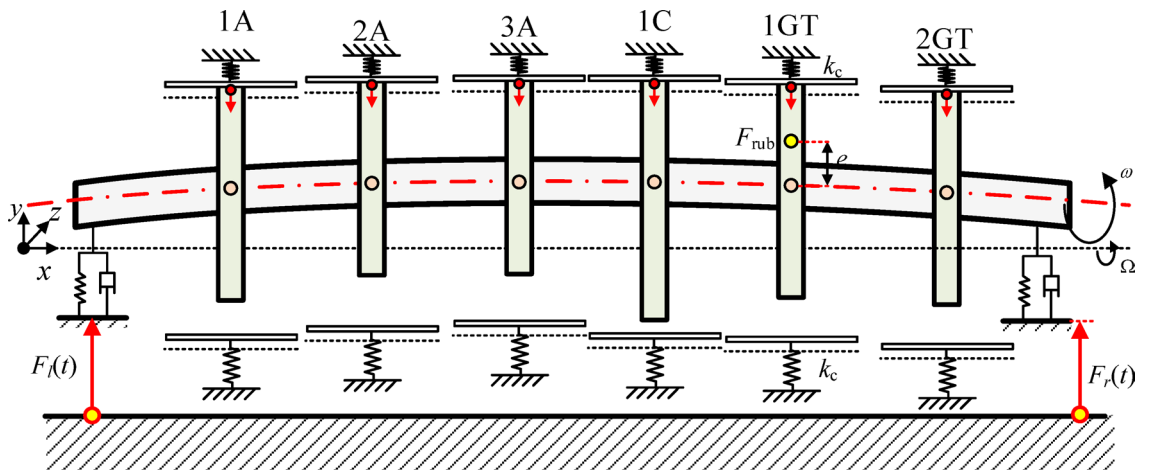


Fig. 13. Schematic diagram of the rub-impact phenomenon in the gas generator rotor under impact excitations.

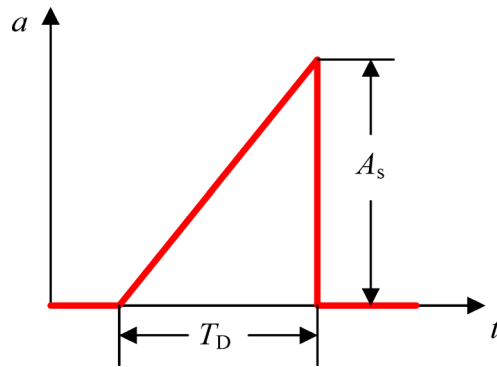


Fig. 14. Sawtooth Pulse Waveform.

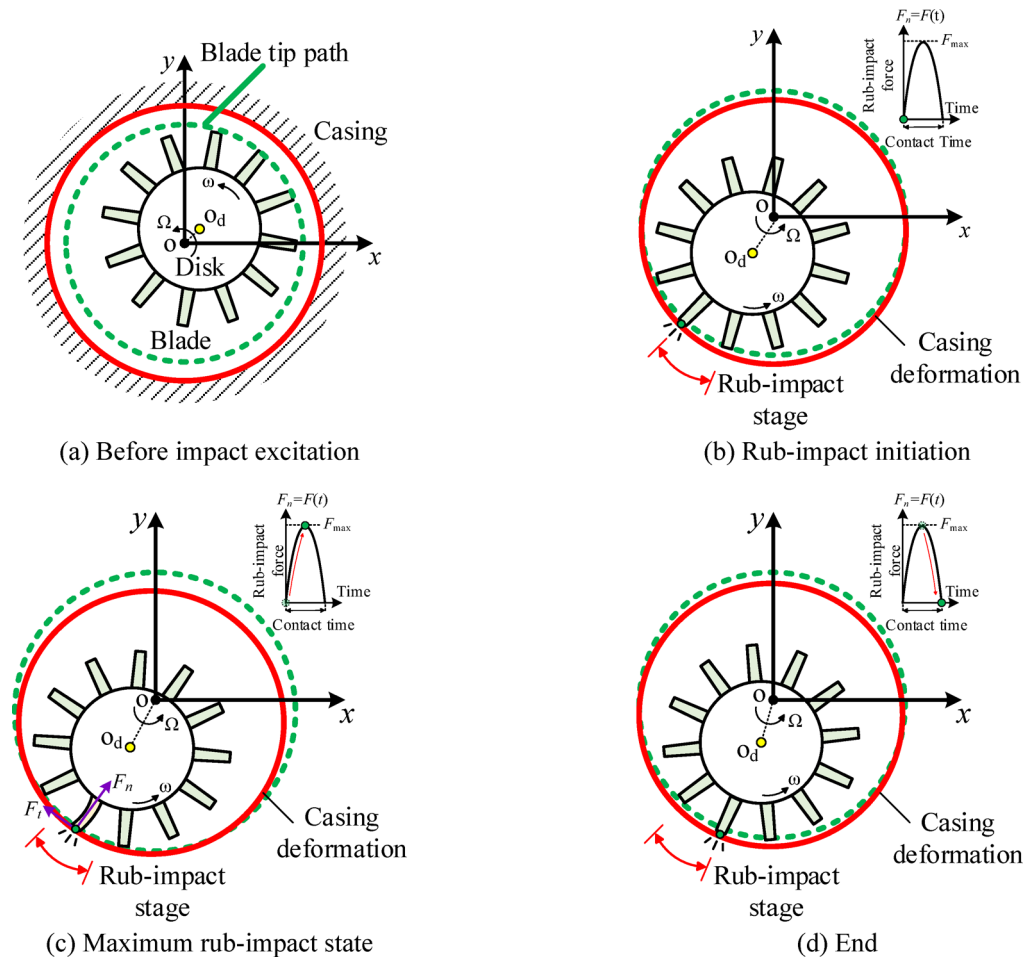
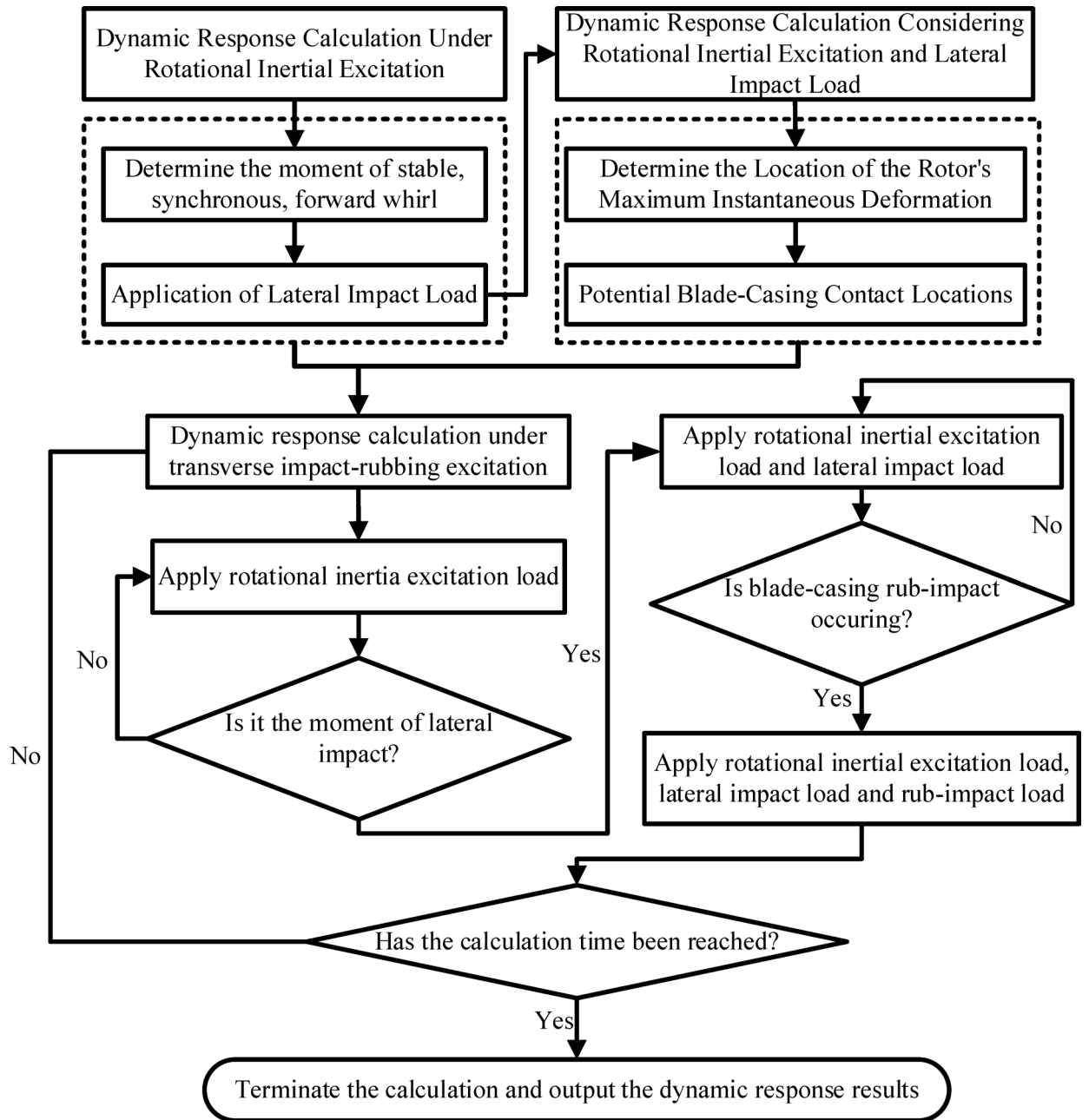


Fig. 15. Schematic diagram of the rub-impact mechanical process between a single blade and casing under impact excitation. (a) Before impact excitation, (b) Rub-impact initiation, (c) Maximum rub-impact state, (d) End.

the casing gradually weakens, the rub-impact force gradually decreases, and finally the contact separates, the rub-impact load drops to zero, and the rub-impact ends (as shown in Fig. 15(d)). With the continuous whirling of the rotor, under the accumulation of unbalance, rub-impact contact between the blade and the casing may occur again.

Substituting Eq. (41) into Eq. (40), the dynamic response of rub-impact excitation for the gas generator rotor system under large impact excitation can be obtained. The specific calculation process is shown in Fig. 16. First, under zero initial conditions, only the rotational inertial excitation load is applied to the gas generator rotor,



**Fig. 16.** Calculation process of dynamic response for gas generator rotor system under impact-rub-impact excitation.

and the fourth-fifth order Runge-Kutta method is used to numerically solve Eq. (42) to calculate its dynamic response.

$$\begin{cases} M_{RCSB}\ddot{q}_{RCSB} + (C_{RCSB} + G_{RCSB})\dot{q}_{RCSB} + K_{RCSB}q_{RCSB} = F_{RCSB} + F_e \\ M_{casing}\ddot{q}_{casing} + C_{casing}\dot{q}_{casing} + K_{casing}q_{casing} = F_{casing} - F_e \end{cases} \quad (42)$$

Through this calculation, determine the response amplitude and the corresponding time when the critical section of the rotor reaches a stable synchronous forward precession state. Use this time as the moment to apply the impact load. Subsequently, under zero initial conditions, recalculate the dynamic response. Apply the rotational inertial excitation load, and at the determined impact moment, apply the impact load to the degrees of freedom of the rotor support according to the selected coordinate system. By analyzing the displacement response of the rotor at the instant of the impact, determine the position with the maximum displacement response to identify the possible rub-impact positions between the blades and the casing. Finally, under zero initial conditions, perform the dynamic response calculation again. Apply the rotational inertial excitation load and the impact

Tie rod	1 A	2 A	3 A	1 C	1GT	2GT
$R_{Lo}=19.5$	$R_{Lo}=45.75$	$R_{Lo}=54$	$R_{Lo}=86$	$R_{Lo}=70$	$R_{Lo}=47.5$	$R_{Lo}=38.5$
$R_{Li}=22$	$R_{Li}=25.4$	$R_{Li}=43$	$R_{Li}=81$	$R_{Li}=57$	$R_{Li}=42.5$	$R_{Li}=32.5$
$L=576$	$R_{Ro}=74.55$	$R_{Ro}=86$	$R_{Ro}=86$	$R_{Ro}=91$	$R_{Ro}=36$	$R_{Ro}=30$
	$R_{Ri}=42$	$R_{Ri}=81$	$R_{Ri}=81$	$R_{Ri}=150$	$R_{Ri}=33.5$	$R_{Ri}=28$
	$h_d=59.55$	$h_d=82$	$h_d=100$	$h_d=120$	$h_d=85$	$h_d=40$
	$h_1=5.56$	$h_1=3$	$h_1=4.5$	$h_1=-$	$h_1=1.5$	$h_1=1.5$
	$h_2=2.56$	$h_2=2$	$h_2=2.5$	$h_2=-$	$h_2=3$	$h_2=3$
	$b_1=66$	$b_1=40$	$b_1=38$	$b_1=-$	$b_1=22$	$b_1=22$
	$b_2=80.38$	$b_2=35$	$b_2=25$	$b_2=-$	$b_2=20$	$b_2=20$
	$L_b=71.56$	$L_b=35$	$L_b=24$	$L_b=-$	$L_b=30$	$L_b=30$

**Table 2.** Structural parameters of the gas generator rotor system(Unit: mm).

Order	No stiffness loss	Only considering the end-tooth contact effect	Considering the bending deformation and the tooth surface contact effect
1st	11,413	11,400	11,377
2nd	25,258	25,098	24,803
3rd	67,930	67,239	66,330

**Table 3.** Critical speeds of a turboshaft engine gas generator rotor system (RPM).

load at the determined impact moment. Simultaneously, based on the previously identified potential rub-impact positions, determine the clearance between the blades and the casing at the impact moment to check if rub-impact occurs (i.e., whether the rotor precession radius exceeds the blade-casing clearance). If the rub-impact condition is met, apply the rub-impact excitation load to the lateral degrees of freedom of the corresponding bladed disk, and further analyze the response amplitude of the rotor during the impact-rub-impact process.

**Numerical example and discussion**

Following the establishment of the rub-impact dynamics model for the gas generator rotor system under impact loads, this section first verifies the equivalent dynamic model of the circular arc end-tooth connection structure. Subsequently, the rotor dynamics modeling approach is validated experimentally, and a simulation is performed to analyze the influencing factors affecting the rub-impact characteristics of the gas generator rotor system under impact excitation. Table 2 presents the structural dimension parameters of the gas generator rotor system investigated in this study.

**Dynamic analysis of circular Arc end-teeth connection structure**

To further illustrate the impact of circular arc end-tooth connection structure stiffness loss on the gas generator rotor system, this section calculates the critical speeds and mode shapes of the gas generator rotor system, as presented in Tables 3 and 4, and compares the results under different levels of stiffness loss. As stated in 2.2, the stiffness loss caused by the circular arc end-tooth connection structure is mainly due to the following three aspects: the change in the area of the circular arc end-tooth contact interface, the change in contact characteristics, and the bending deformation of the rotor. This section will gradually consider the influence of these factors on simulation calculations.

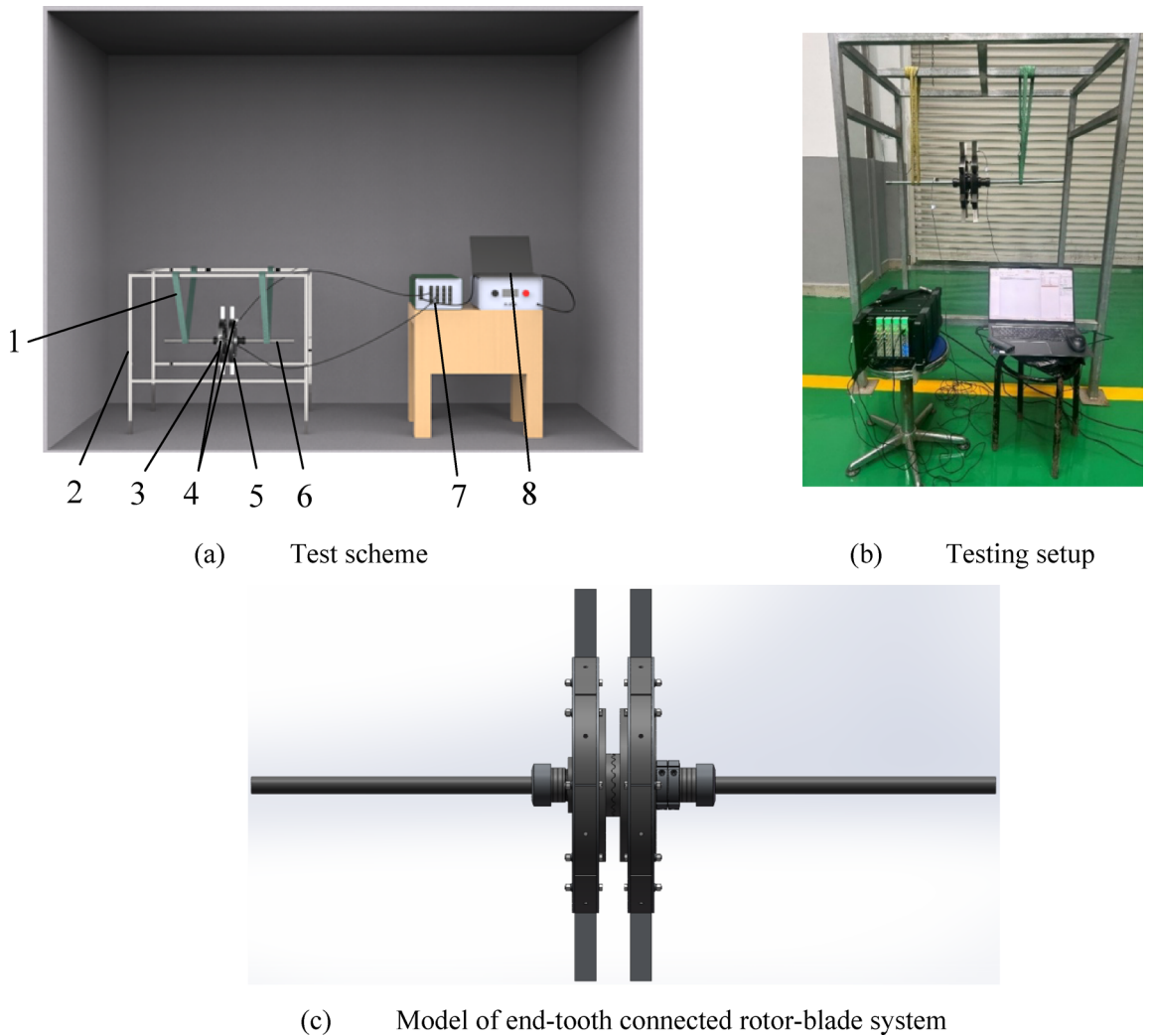
As demonstrated in Table 3, considering only the contact characteristics of the end-tooth interface results in minimal changes to the first three critical speeds of the rotor system. The third critical speed exhibits the largest change, decreasing by approximately 1.02% relative to the baseline case without stiffness loss. After considering the bending deformation of the rotor system, it has a significant impact on the second and third-order critical speeds of the gas generator rotor system, which are decreased by 1.8% and 2.36% respectively. This may lead to a reduction in the margin between the maximum operating speed and the first-order critical bending speed during the actual operation of the gas generator rotor. Therefore, a dynamic model incorporating the loss of bending stiffness in the circular-arc end-tooth connection structure is necessary to accurately describe the rub-impact response characteristics of the rotor-casing system under external impact loads.

**Modal testing of the circular Arc end-teeth connection rotor system**




To carry out the experimental verification research on the vibration characteristics of the circular arc end-tooth connected rotor system, this study designs a rotor-blade vibration characteristic test with end-tooth connection based on the dynamic similarity design principle and according to the structural characteristics of the disk assembly and blade assembly in the gas generator rotor system. The specific structural schematic diagram is shown in Fig. 17. The test system mainly consists of the following components: (1) Flexible suspension ropes, (2) Support frame, (3) Bladed disk I, (4) Vibration acceleration sensor, 5 – 1. Bladed disk II, 6. Rotor, 7. Data acquisition device, 8. Laptop computer.

Order	No stiffness loss	Only considering the end-tooth contact effect	Considering the bending deformation and the tooth surface contact effect
1st			
	Translational mode (190.2)	Translational mode (190.2)	Translational mode (189.5)
2nd			
	Pitch mode (420.9)	Pitch mode (418.3)	Pitch mode (413.4)
3rd			
	Bending mode (1123.2)	Bending mode (1122.2)	Bending mode (1105.5)

**Table 4.** Vibration modes of a turboshaft engine gas generator rotor system in rotating state (Hz).



**Fig. 17.** Modal test scheme for end-tooth connected rotor-blade system.

Instrument	Type	Parameter	Usage	Physical diagram
Hammer	LC02	Sensitivity: 1 mV/N Range: 5000 N Size: 230 mm Mass: 158 g	Generate excitation	
Acceleration sensor	4335-B-001	Range: 0.3 Hz ~ 10 kHz Sensitivity: 1 mv/ms <sup>2</sup> Mass: 6 g	Collect vibration acceleration signals	
Signal acquisition and analysis system	3050-A-060	Frequency range: 0 Hz ~ 51.2 kHz	Receive force signals and acceleration signals	

**Table 5.** Test instrument.

	Rotor	Disk	Blade	End-teeth	Coupling
Density (kg/m <sup>3</sup> )	8140	8140	8700	8240	8140
Young's modulus (GPa)	225	225	131	204	207
Shear modulus (GPa)	83.3	83.3	46.16	78.46	80.23
Poisson's ratio	0.35	0.35	0.419	0.3	0.29
Inner diameter (mm)		20		65	
Outer diameter (mm)	20	300		74	
Pitch circle radius (mm)				20	
Length (mm)	830	33	80		
Thickness (mm)		60	2		
Number of parts	1	2	10	20	1

**Table 6.** Dimensions and material parameters of experimental workpieces for the end-teeth connected rotor blade system.

A hammer-impact modal test was performed on the circular arc end-teeth connection rotor–blade assembly to validate the mass and stiffness matrices derived in the dynamic model. To isolate structural matrices from boundary effects, the assembly was suspended on flexible cords, approximating a free–free condition.

The test scheme is shown in Fig. 17(a), with the specific procedures as follows: (1) Construct a finite element mesh model of the end-tooth connected rotor-blade system using finite element simulation software; (2) Import the mesh model into B&K PLUSE vibration and noise measurement analysis software; (3) Connect the test equipment sequentially according to the scheme; (4) Set parameters for excitation points and measuring points in PLUSE software; (5) Perform successive hammer excitations on the excitation points of the test piece; (6) Collect acceleration frequency-domain response signals via acceleration sensors arranged at the measuring points; (7) Process the test data in PLUSE software; (8) Organize the equipment and clean the test site to complete the experiment. It should be noted that to eliminate accidental errors, the test is conducted twice to ensure result reliability, with the field photo shown in Fig. 17(b). The test equipment and relevant parameters are listed in Table 5.

In this experiment, the test piece uses two sets of disk-blades to simulate the turbine structure. For ease of machining, the blades in this experiment are simplified into rectangular plate structures in cross-section. The relevant material parameters and geometric dimensions of the test piece are shown in Table 6. The basic design parameters of the end-tooth connection structure are as follows: outer diameter  $d_{\text{outer}} = 74$  mm, inner diameter  $d_{\text{inner}} = 65$  mm, pressure angle of 30°, number of teeth of 20, addendum height of 1.98 mm, dedendum height of 1.48 mm, and addendum chamfer height of 0.3 mm.

Following the test scheme outlined previously, this experiment was conducted. The test workpiece was suspended from a metal support using an elastic nylon rope, as illustrated in Fig. 17. Repeated impacts were applied to various excitation points on the rotor, disk, and blades, and the resulting structural acceleration response signals were collected. This data was then used to generate acceleration frequency response curves for the end-tooth connected rotor-blade system under free boundary conditions, as shown in Fig. 18. The acceleration frequency response curves reveal a concentration of peaks in certain regions, hindering the clear identification of corresponding natural frequencies. To address this, the first five resonant frequency regions are presented as local enlargements in Fig. 19. As previously noted, to ensure reliable test results, the frequencies of peak points exhibiting close values in the two tests were averaged to determine the final experimental results. A comparison of the first five natural experimental frequencies is presented in Fig. 20.

Figure 20 demonstrates a strong correlation between the predicted results obtained using the method presented in this paper and the experimental test results. The maximum relative error is 2.95%, occurring at the fifth order frequency, while the minimum relative error is 1.49%, occurring at the second order frequency.

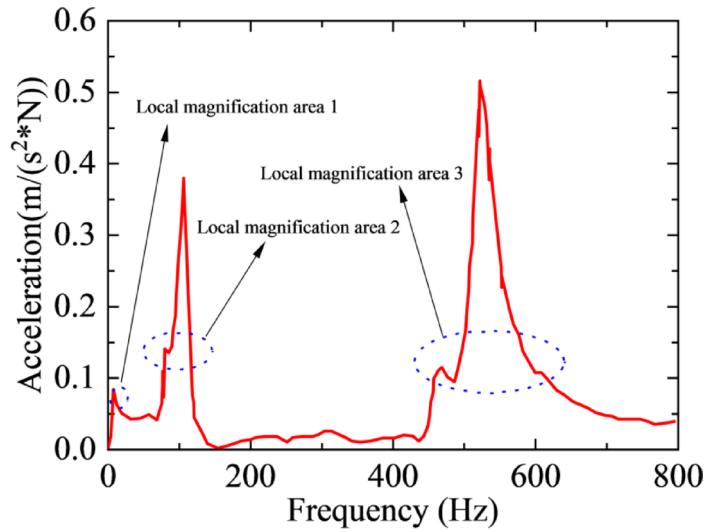
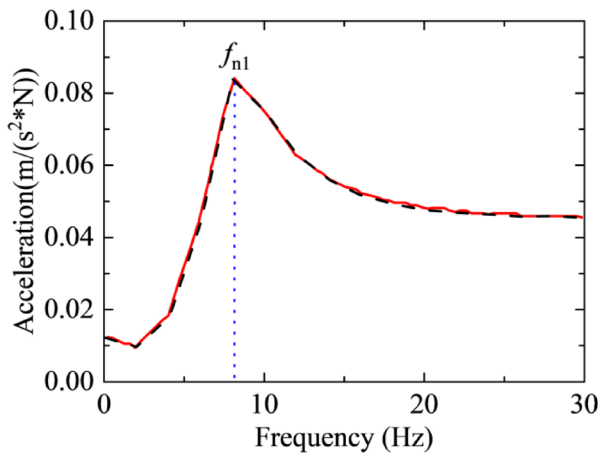
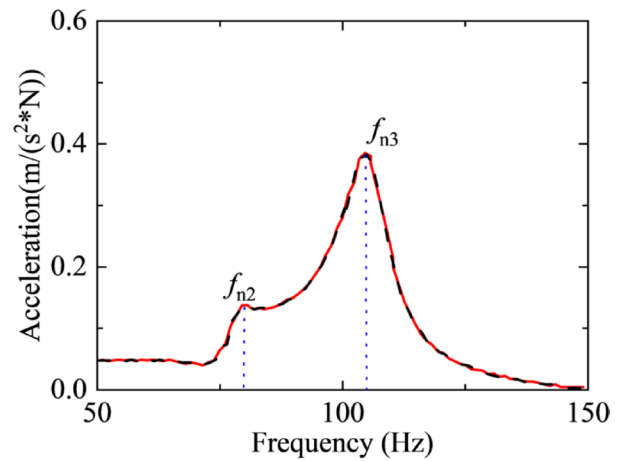


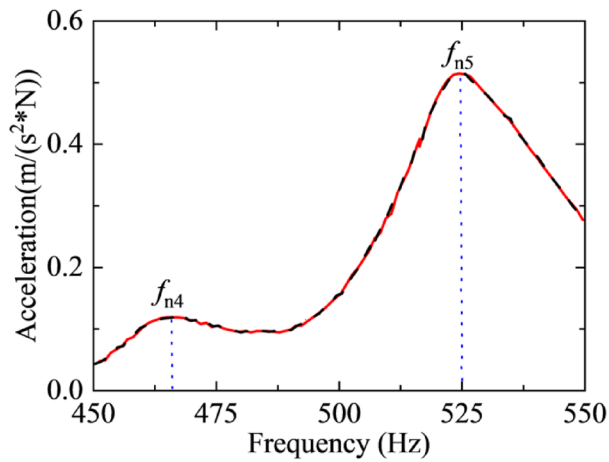
**Fig. 18.** The acceleration frequency response curve of the end-tooth connected rotor-blade system with free boundary conditions.



(a) Local magnification area 1



(b) Local magnification area 2



(c) Local magnification area 3

**Fig. 19.** Acceleration frequency response curve in different local magnification areas. (c) Local magnification area 3.

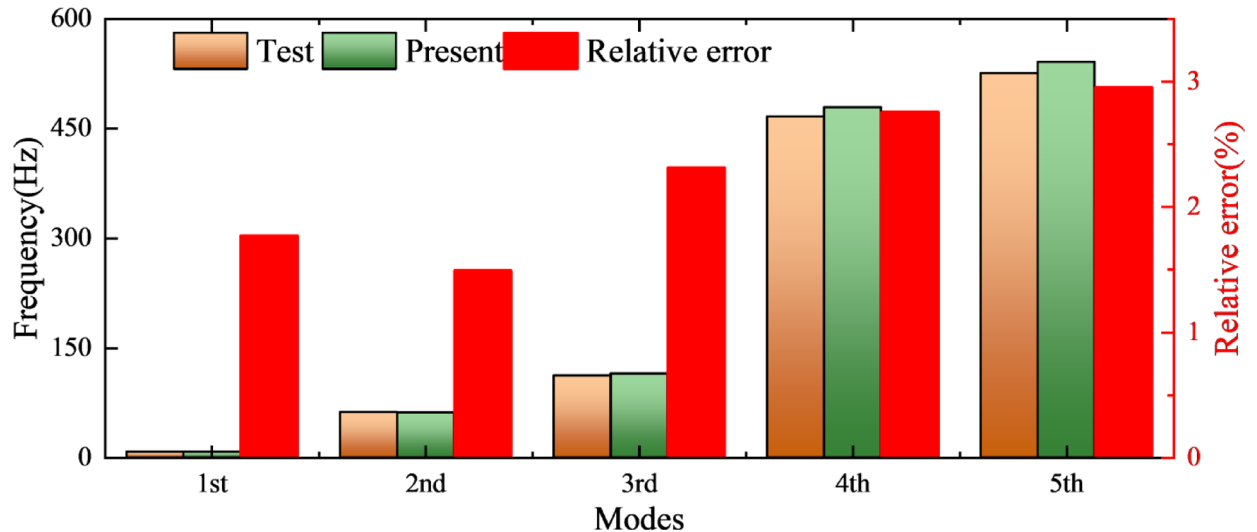


**Fig. 20.** Comparison of the first 5-order natural frequencies (Hz) of the end-tooth connected rotor-blade system under free boundary conditions.

This indicates that the construction of related matrices, such as the mass matrix and stiffness matrix, during the dynamic modeling of the circular arc end-teeth connection rotor-blade system is accurate. Furthermore, Fig. 18 also reveals the presence of other, less prominent peaks within the analysis frequency range of [200, 400] Hz, in addition to the peak values marked in Fig. 19. This phenomenon primarily arises from the inclusion of other components, such as couplings, within the arc-shaped gear connection rotor-blade system, which can also excite their inherent frequencies during testing.

### Analysis of the rub-impact response of the gas generator rotor system under impact excitation

This section will analyze the rub-impact response of the gas generator rotor system under large impact excitation. Given that the operating environment of the first-stage gas turbine rotor (1GT) and the first-stage blade disk rotor (1 A) is the most severe and exhibits the smallest tip clearance, the rub-impact loads generated at 1GT and 1 A are primarily referenced when considering blade-casing rub-impact excitation.

The rub-impact analysis was carried out for the gas turbine engine rotor blade-casing system, considering impact loads during obstacle crossing in road driving. The rotor system is configured with a support stiffness of  $1.5 \times 10^7$  N/mm, support damping of 2000 N-s/m, a rub clearance of 0.03 mm for 1GT, and a rub clearance of 0.15 mm for 1 A, the operating rotational speed is 45,000 rpm. The analysis first considers an impact load typical of road driving, with a duration of  $T_D=0.191$ s and an impact acceleration of  $A_s=2.359$  g.

Inserting the impact load into Eq. (41) yields the time-domain displacement histories of the first-stage turbine disk and its bladed sector (Fig. 21). The green trace in panels (a) and (b) denotes the blade-tip clearance. Under off-road shock, the 1GT blades intermittently contacted the casing, whereas the 1 A compressor disk did not; blade-case rubbing continued after the excitation had ceased.

Due to the relatively low amplitude of the impact and the damping effect of the support system, severe rub-impact instability was avoided.

Next, the dynamic response to a short-duration, high-amplitude impact typical of tank gun firing is analyzed. The parameters for this impact are an amplitude of  $A_s=20$  g and a duration of  $T_D=11$  ms. All other rotor structural parameters are the same as in Fig. 21. The displacement time-domain responses and shaft orbits of the first-stage disk (1 A) and first-stage gas turbine (1GT) in the rotor-blade-casing system are shown in Fig. 22.

As revealed by Fig. 22, the impact from artillery fire induced a significant rub-impact at the gas turbine rotor. The peak displacement of 1 A was 0.215 mm, which is 143.3% of the design clearance (0.15 mm), but after the impact is over, the rotor does not exceed the design clearance. The peak displacement of 1GT reached 0.096 mm, exceeding its 0.03 mm clearance by 3.2 times. After the load ends, due to the vibration energy dissipation characteristics of the gas turbine rotor, the displacement response remains in the range of 0.04–0.05 mm, and continues to break through the casing clearance constraint, resulting in the first-stage blade disk rotor displacement response increasing by 39% compared to before the rubbing.

Gun-fire-induced shocks generate large transient displacements that trigger sustained rub-impact in the 1GT turbine rotor while sparing the 1 A compressor disk. The resultant motion amplification transmitted to the compressor disk underlines the necessity of analyzing fully coupled rotor dynamics.

### Parametric study

The previous section presented the simulation results for the rub-impact response of the gas generator rotor system under a specific impact excitation. Building on those findings, this section performs a parametric study to systematically analyze how key structural characteristics influence the rub-impact response of the gas

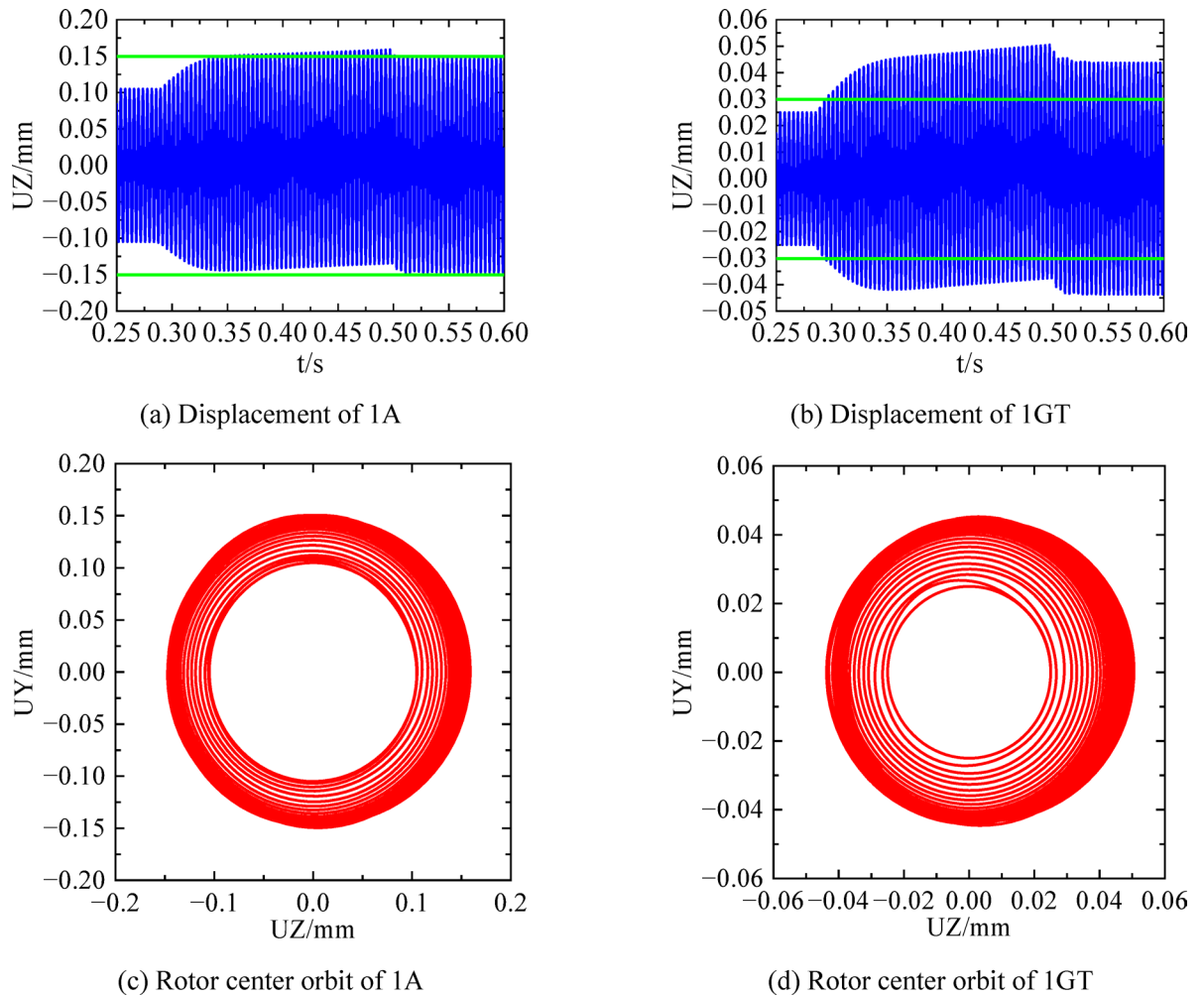


**Fig. 21.** The rub-impact response of the gas generator rotor system under driving impact excitation.

generator rotor at operating speed (45000 rpm). By varying a single parameter at a time, we can isolate its effect and determine the sensitivity of the rotor's dynamic behavior to changes in that parameter.

This parametric study employs the high-amplitude impact load characteristic of artillery firing as its baseline condition, a scenario previously demonstrated to induce severe rub-impact. The structural parameters examined include impact load amplitude, rotor support damping, blade-casing stiffness, rotor-casing clearance, and rotor unbalance. The resulting findings are essential for establishing design and optimization principles to enhance the impact resistance of the gas generator rotor system.

#### *Influence of impact load amplitude on the rub-impact response of the gas generator rotor system*

As indicated in the research of Sect. “[Analysis of the rub-impact response of the gas generator rotor system under impact excitation](#)”, the impact load generated during road driving does not exceed 5 g, which has a limited effect on the rub-impact characteristics of the gas generator rotor system. After a short dynamic transition process, the gas generator rotor system can gradually return to its initial steady-state operation. However, for the strong impact load during artillery firing, although its duration is short, the severe load amplitude has a significant impact on the gas generator rotor system. Therefore, this subsection further investigates the rub-impact response characteristics of the system under different impact load amplitudes.

The gas generator rotor system is specified with the following parameters: the support stiffness is  $1.5 \times 10^7$  N/m, the support damping is 2000 N·s/m, and the equivalent rub-impact stiffness is  $1 \times 10^8$  N/m. The rub-impact clearance is set to 0.15 mm for 1 A and 0.03 mm for 1GT. The unbalanced amounts are set to 10 g·mm for both the 1 A and 2GT. Figure 23 shows the displacement time-domain response curves of the gas generator rotor system for different impact load amplitudes, with C1 to C4 corresponding to 10 g, 20 g, 30 g, and 40 g, respectively. The green shaded area consistently represents the safe operational region within the blade-casing clearance, where rub-impact is avoided. As can be observed from the figure, the rotor displacement response increases with the increasing impact load. The maximum rub-impact displacement response of 1 A increases from 0.017 mm to 0.29 mm, while the maximum displacement of the gas turbine rotor increases from 0.055 mm to 0.12 mm. Although the impact displacement response of 1 A is larger, the 1GT is more prone to rub-impact under impact loads due to its very small rub clearance. Furthermore, as the impact load increases, the number of

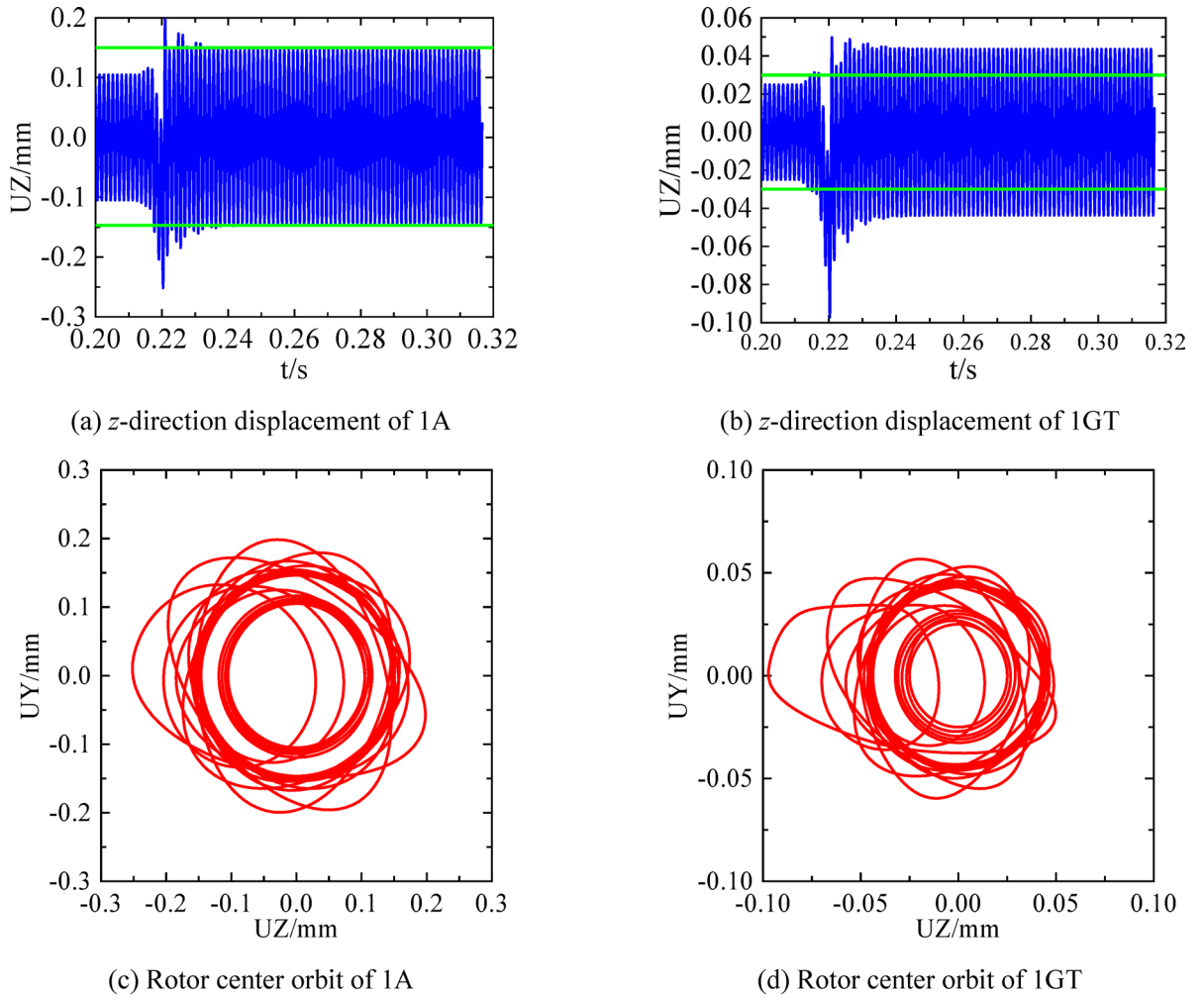


**Fig. 22.** The rub-impact response of the gas generator rotor system under the launching impact excitation of artillery.

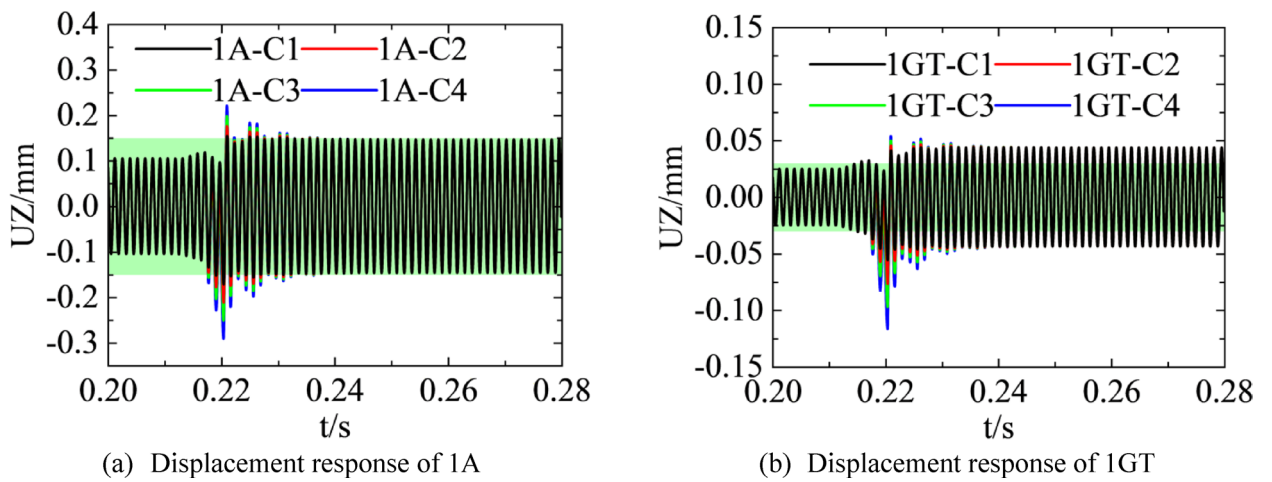


**Fig. 23.** Displacement response of 1 A and 1GT under different impact loads.

times the rotor's post-impact displacement response exceeds the clearance limit also increases, indicating a rise in the number of rub-impact events and a heightened risk of instability.

Figure 24 depicts the rotor center orbits for the 1 A and 1GT disks under varying impact loads, illustrating the corresponding motion paths of the gas generator rotor. The orbits show that the rotor's motion path changes significantly as the impact load increases, with the eccentricity becoming more pronounced and the vibration amplitude growing substantially. Notably, the 1GT rotor exhibits clear instability under higher impact loads. This instability is reflected in the irregularity of its motion path and may compromise the stability and reliability of the entire rotor system. To mitigate this issue, effective vibration isolation for the gas turbine engine should be implemented through the tank's suspension and support structure, for instance, by employing advanced vibration isolation materials or active suspension systems to absorb and isolate external impact loads, thereby mitigating damage from rotor rubbing during combat operations.

#### *Influence of support damping on the rub-impact response of the gas generator rotor system*

The parameters of the SFD significantly govern the response amplitude of the gas generator rotor. The influence of support stiffness was found to be negligible under impact excitation, as it primarily affects the system's natural frequency and has limited effect on the response at non-critical speeds. Therefore, this section focuses on investigating the influence of support damping on the rub-impact response of the gas generator rotor system under impact excitation. The unbalance of both the first-stage blade disk (1 A) and the second-stage turbine (2GT) is set at 10 g-mm; support stiffness is  $1.5 \times 10^7$  N/m; equivalent rub-impact stiffness is  $1 \times 10^8$  N/m; rub clearances are 0.15 mm in the compressor section and 0.03 mm in the turbine section; and the shock excitation amplitude is 20 g. Time-domain rub-impact responses and rotor center orbits of the gas-generator rotor are analyzed for support damping values of 500, 1000, 1500, and 2000 N-s/m, as presented in Figs. 25 and 26.

The legend suffixes N1 to N4 represent support damping of 500 N-s/m, 1000 N-s/m, 1500 N-s/m, and 2000 N-s/m, respectively. Analysis of the time-domain response demonstrates that increased damping significantly reduces the peak response amplitude, consequently lowering the probability of blade-casing contact. Higher support damping accelerates the vibration decay rate and substantially shortens the recovery time. This occurs because damping promotes energy dissipation, allowing the system to return to a stable state more rapidly. Conversely, insufficient support damping demonstrates adverse effects: the resulting increase in response amplitude promotes more frequent rotor-stator rubbing events. This correlation arises because inadequate damping fails to dissipate vibration energy effectively, permitting rotor displacements to exceed safe operational limits. Therefore, to ensure stable operation of the gas generator rotor system, the support damping should be maintained at or above 2000 N-s/m.

#### *Influence of blade-casing stiffness on the rub-impact response of the gas generator rotor system*

Blade-casing stiffness critically dictates the deformation behavior during rubbing. Higher stiffness constrains deformation, potentially raising contact forces and local stresses. Conversely, lower stiffness allows greater deformation, which may dissipate energy but also prolong contact or increase contact area, complicating the system's dynamics and wear. Consequently, optimizing blade-casing stiffness is essential for robust turbomachinery design. Following this analysis, this section will examine the influence of stiffness on rubbing response under maneuver-induced impacts.

Based on the allowable range of structural parameters for the gas generator rotor system studied in this paper, an imbalance of 10 g-mm was applied to both 1 A and 2GT, the support stiffness was set to  $1.5 \times 10^7$  N/m,

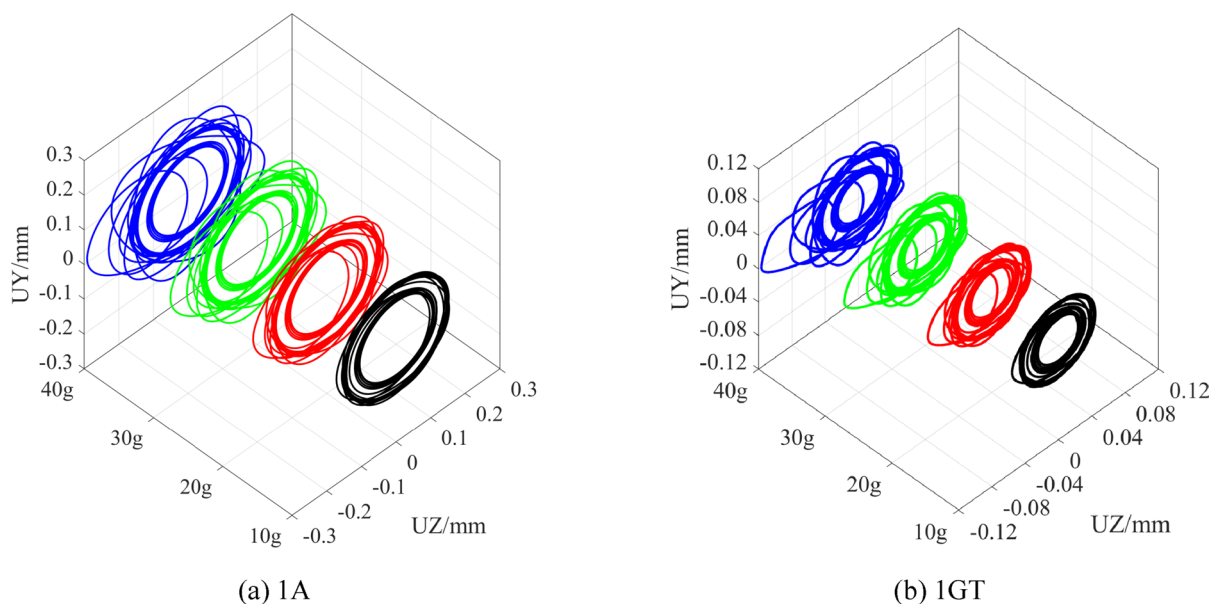


**Fig. 24.** The rotor center orbit of 1 A and 1GT under different impact loads.

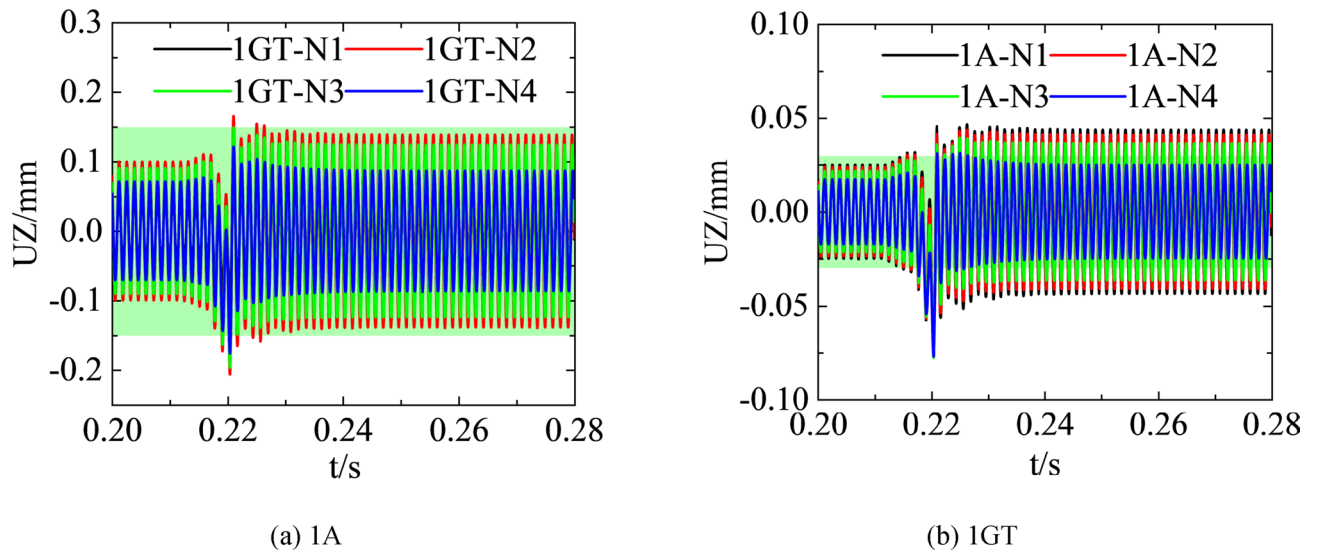


**Fig. 25.** Displacement response of 1 A and 1GT under different support damping.

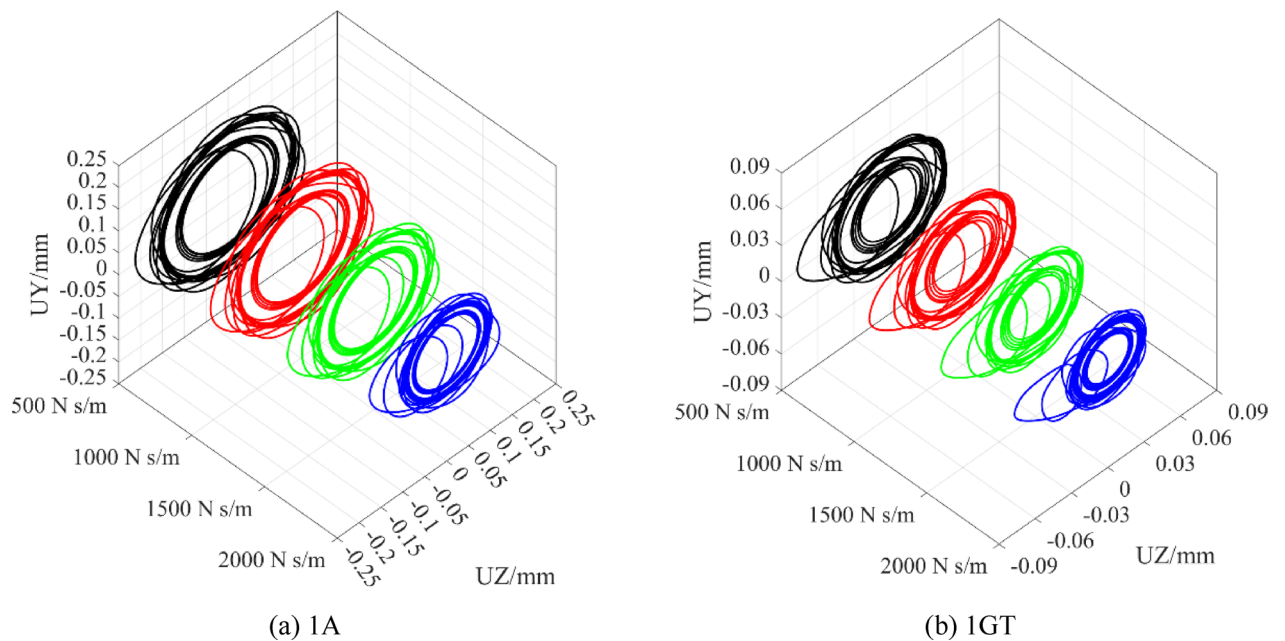


**Fig. 26.** The rotor center orbit of 1 A and 1GT under different support damping.

the rotor rubbing clearance in 1 A was 0.15 mm, and in 1GT was 0.03 mm. An impact excitation amplitude of 20 g was applied. The time-domain responses and axial trajectories of the rotor under rub-impact conditions for different blade-casing stiffness were analyzed, with specific results shown in Figs. 27 to 28. In Fig. 27, the suffixes K1 to K4 in the legend represent rubbing stiffness values of  $2.5 \times 10^7$  N/m,  $5 \times 10^7$  N/m,  $7.5 \times 10^7$  N/m, and  $10 \times 10^7$  N/m, respectively.

From the time-domain vibration responses and shaft orbits, it is evident that rub-impact stiffness has a significant effect on the gas generator rotor's rub-impact response. As the rub-impact stiffness decreases, the amplitude of the rotor's response increases, and the range of the shaft orbit expands accordingly. Comparing the maximum stiffness K1 to the minimum stiffness K4, the maximum rub-impact response amplitude of 1 A under the impact load decreases by 9.91%, with the post-impact response peak reducing by 18.37%. For 1GT, the maximum response amplitude under the impact load is reduced by 13.16%, and the post-impact response peak decreases significantly by 30.23%. This indicates that a higher rub-impact stiffness can effectively limit the rotor's displacement during the rub-impact process.

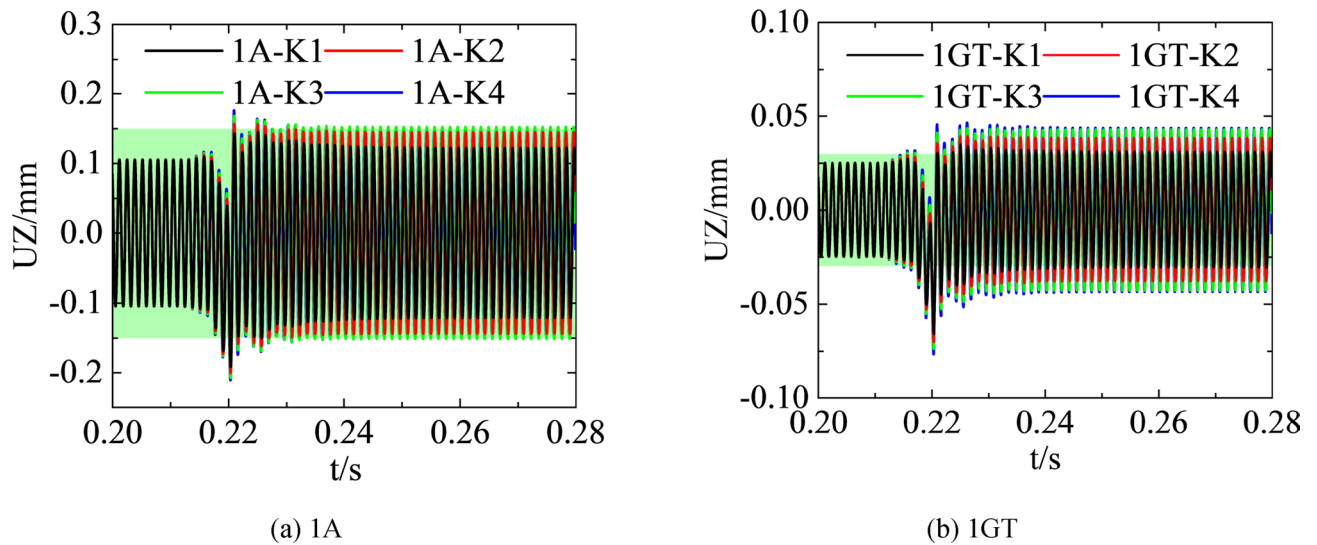


**Fig. 27.** Displacement response of 1A and 1GT under different blade-casing stiffness

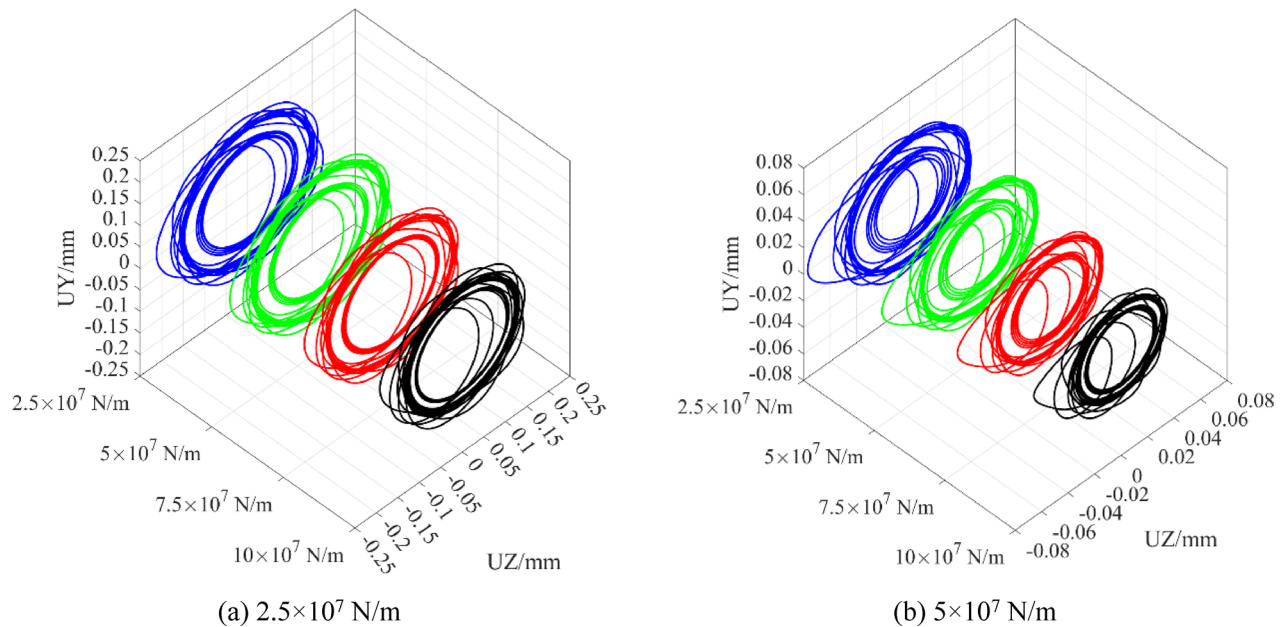


**Fig. 28.** The rotor center orbit of 1A and 1GT under different blade-casing stiffness.

Therefore, it is recommended to reduce the effective rub-impact stiffness through composite bushings or flexible supports to suppress the peak contact force; meanwhile, for high-stiffness casing systems, the tip clearance can be expanded (120% to 150% of the design value) to prevent impact rub-impact instability.

#### *Influence of blade-casing clearance on the rub-impact response of the gas generator rotor system*

The blade-casing clearance significantly affects the rub-impact response of the gas generator rotor system. A smaller clearance restricts rotor eccentric displacement, increasing the probability of rotor-stator contact and leading to amplified vibration amplitudes and accelerated wear. Conversely, a larger clearance compromises engine aerodynamic efficiency and power output. This section investigates the influence of clearance size on the rub-impact response characteristics of the rotor system under shock excitation. Figures 29 to 30, 31 present the time-domain responses and rotor center orbit under varying blade-casing clearances.

In Fig. 29, the legend suffixes X1 through X4 represent rubbing clearances of 0.01 mm, 0.03 mm, 0.05 mm, and 0.07 mm, respectively. Analysis reveals that when the rubbing clearance ranges from 0.01 to 0.03 mm, the actual gap between the rotor and casing is minimal, increasing the likelihood of synchronous circumferential rubbing under external impact excitation. Consequently, the peak vibration response of the rotor increases significantly. With larger blade-tip clearances, rubbing typically manifests as partial contact—characterized

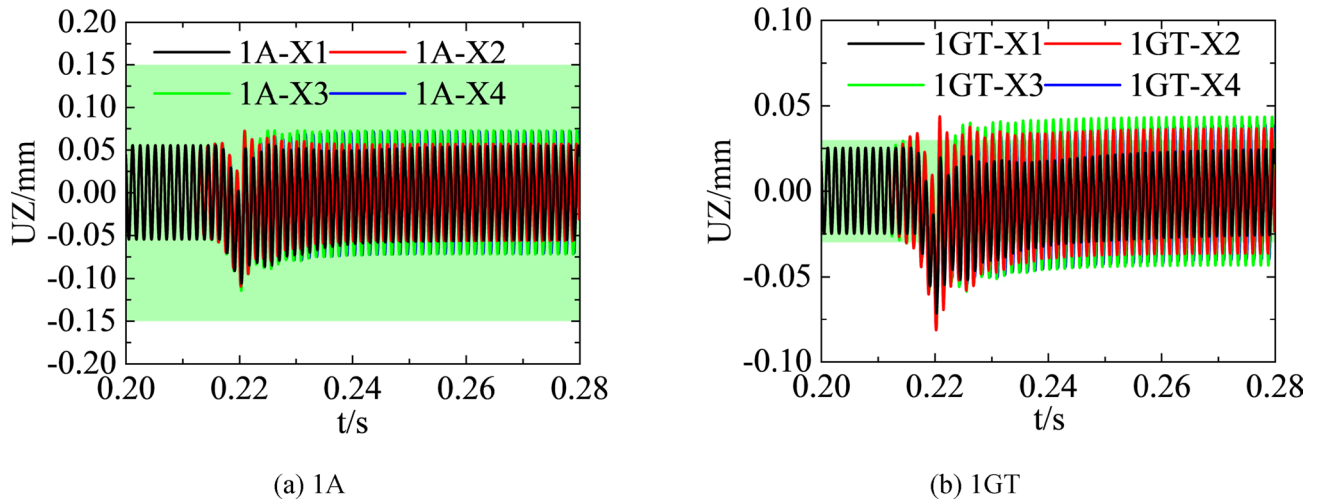


**Fig. 29.** Displacement response of 1A and 1GT under different blade-casing clearance

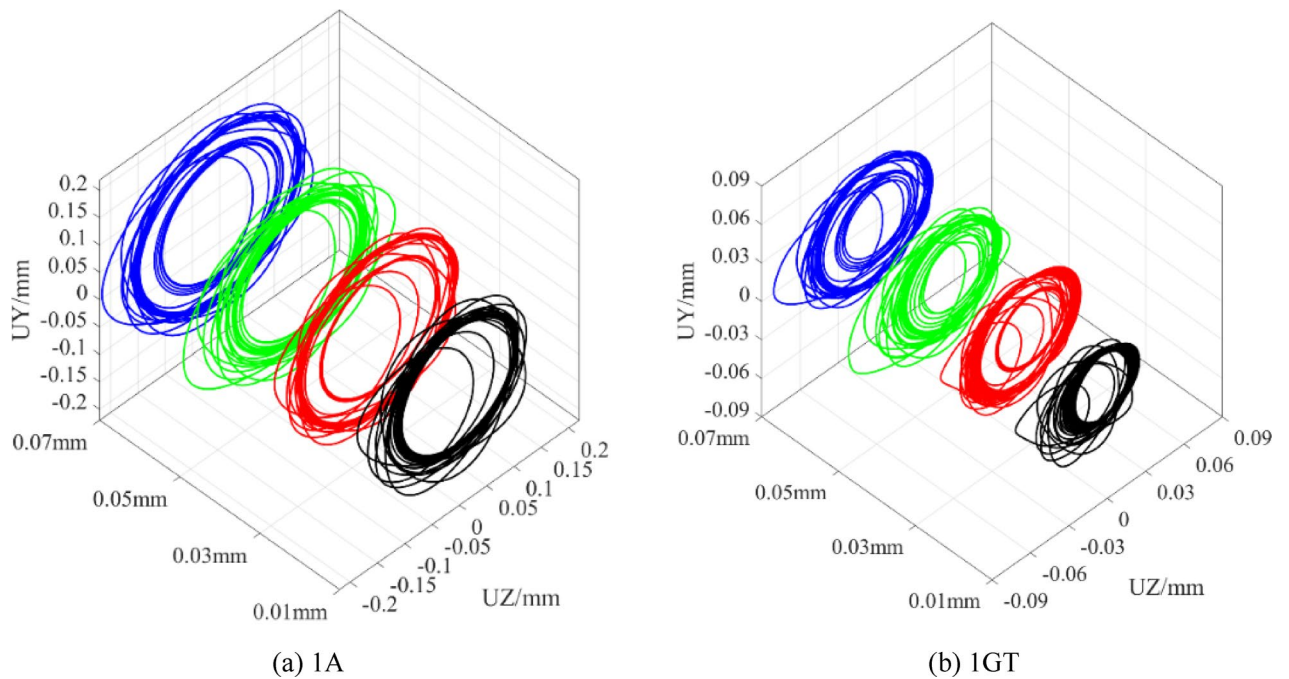


**Fig. 30.** The rotor center orbit of 1A and 1GT under different blade-casing clearance.

by intermittent rotor-casing interaction—which ceases upon the removal of impact excitation. Orbit diagram analysis confirms that larger clearances correspond to a diminished rotor response. The established rub-impact model and response characteristics reveal that both the rub clearance and equivalent rub stiffness collectively govern the intensity of the rub excitation. An appropriate matching of these two parameters can effectively improve post-rub vibration stability and mitigate rubbing-induced damage. Furthermore, the incorporation of abrasion-resistant materials or specialized coatings in the casing design can reduce damage to both the rotor and casing caused by rubbing.

#### *Influence of unbalanced mass on the rub-impact response of the gas generator rotor system*

During the operation of a gas generator, factors such as wear and corrosion of blade surfaces, deposition of particles like sand and metal shavings in the inlet airflow, and sludging/scaling caused by impurities (e.g., moisture and carbides) in lubricating oil leading to local oil accumulation continuously alter the mass distribution of the rotor, thereby leading to an unbalanced response. The unbalanced centrifugal load generated by residual unbalance serves as the primary excitation source driving the rotor's dynamic response. This excitation directly determines the amplitude of rotor bending vibration, which in turn affects the actual rubbing depth between

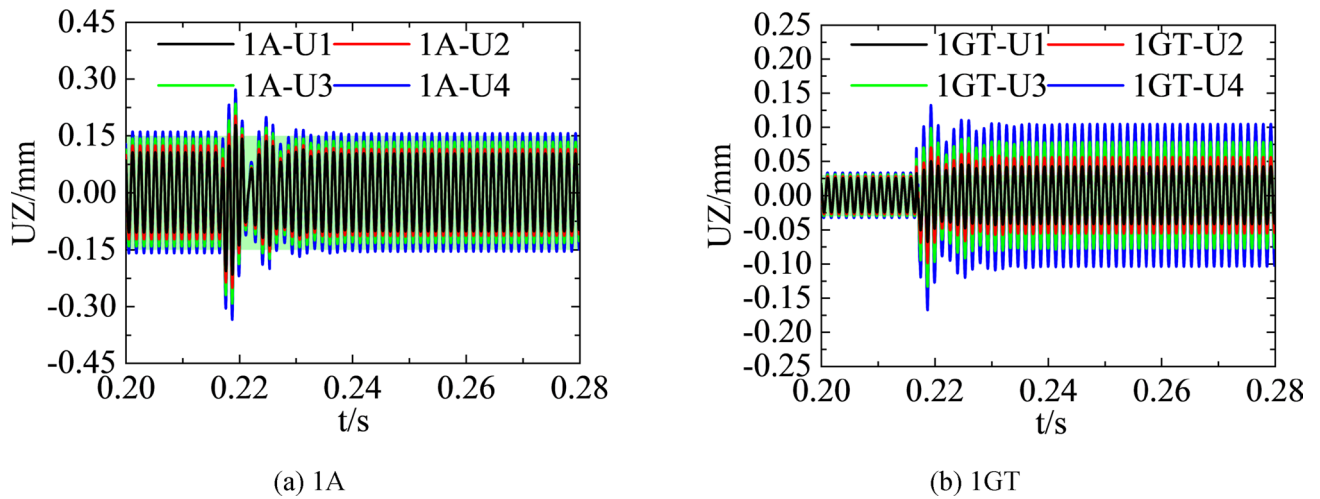


**Fig. 31.** Displacement response of 1A and 1GT under different unbalance mass

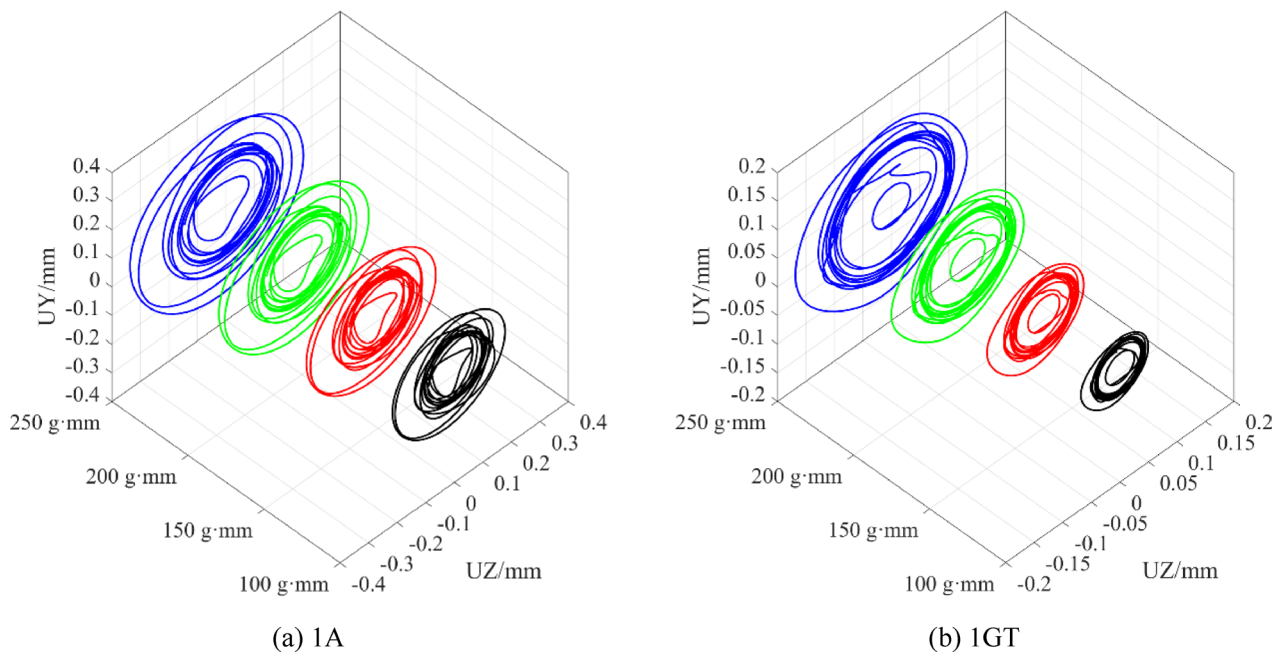


**Fig. 32.** The rotor center orbit of 1A and 1GT under different unbalanced masses.

blades and the casing under high-impact conditions. Thus, residual unbalance is a key influencing factor for the rubbing response of the gas generator rotor system.

During the study, the residual unbalance of the gas generator rotor was set to vary within the range of 100 g·mm to 250 g·mm, with a rubbing clearance of 0.05 mm, an equivalent rubbing stiffness of  $10 \times 10^7$  N/mm, a fixed rotational speed of 45,000 r/min, and an impact excitation amplitude of 20 g. Based on the rubbing dynamics model of the rotor system established in this paper, the motion state of the rotor system after impact-induced rubbing was analyzed. The calculation results are shown in Figs. 34, 35 and 36, where U1, U2, U3, and U4 represent residual unbalances of 100 g·mm, 150 g·mm, 200 g·mm, and 250 g·mm, respectively.

As indicated in the figures, with the increase of residual unbalance, the rubbing depth of the gas generator rotor increases from 0.05 mm to 0.15 mm. Notably, the shaft center orbit after rubbing consistently exhibits obvious synchronous full-circle rubbing (see Figs. 32). When the residual unbalance changes from 100 g·mm to 250 g·mm, the vibration response of the rotor before rubbing increases slightly, while that after rubbing increases significantly. Specifically, when the residual unbalance is 250 g·mm, the maximum rubbing depth reaches 0.15 mm. In summary, the increase in rubbing depth caused by larger residual unbalance exacerbates the hazard of rubbing. Therefore, in engineering practice, to mitigate the risks of rotor rubbing faults, it is necessary to minimize the residual unbalance value, in addition to controlling the magnitude of rubbing loads.

## Conclusion

This paper investigates the rub-impact response characteristics of the gas generator rotor system under impact excitation, providing a theoretical basis for the optimal design of rub-impact in the gas generator rotor system of aero-derived gas turbines. The main conclusions of this study are as follows:

(1) As the impact load increases, the number of rub-impact occurrences of the rotor after the impact also increases, leading to a higher risk of instability.

(2) With the increase of support damping, the time required for the rotor to return to normal operating state is significantly shortened. In practical gas generator rotor systems, modifying or designing support damping is a more feasible engineering measure compared to altering other parameters. To ensure the stable operation of the gas generator rotor system, the support damping is recommended to be no less than 2000 N-s/m.

(3) The blade-casing clearance and blade-casing stiffness jointly determine the rotor rub-impact excitation. Excessive clearance will damage the engine's aerodynamic performance and cause power loss, while reasonable blade-casing stiffness parameters can enhance the vibration stability of the rotor support system and reduce the harm of rub-impact.

(4) The study shows that residual unbalance significantly increases the risk of rotor rubbing faults. As unbalance increases, the rotor's vibration amplitude and rubbing depth also increase, which in turn exacerbates the severity of rub-impact. Therefore, controlling residual unbalance is a critical factor for ensuring the safe operation of the rotor system under high-impact conditions.

## Data availability

Data is provided within the manuscript or supplementary information files.

Received: 15 August 2025; Accepted: 6 October 2025

Published online: 12 November 2025

## References

- Prabith, K. & Krishna, I. R. P. The numerical modeling of rotor-stator rubbing in rotating machinery: a comprehensive review. *Nonlinear Dyn.* **101** (2), 1317–1363 (2020).
- Ma, H. et al. A review on dynamic characteristics of blade-casing rubbing. *Nonlinear Dyn.* **84** (2), 437–472 (2015).
- Dai, X., Jin, Z. & Zhang, X. Dynamic behavior of the full rotorstop rubbing: numerical simulation and experimental verification. *J. Sound Vib.* **251** (5), 807–822 (2002).
- Yu, J. J. On occurrence of reverse full annular rub. in *Turbo Expo: Power for Land, Sea, and Air*. 54662: pp. 219–227. (2011).
- Zhang, H. & Chen, Y. Bifurcation analysis on full annular Rub of a nonlinear rotor system. *Sci. China Technological Sci.* **54**, 1977–1985 (2011).
- Yuan, Z. et al. Influence of rotor's radial rub-impact on imbalance responses. *Mech. Mach. Theory.* **42** (12), 1663–1667 (2007).
- Fay, R., Kreuzer, D. & Liebich, R. *The influences of thermal effects induced by the light-rub against the brush seal to the rotordynamics of turbo machines*. in *Turbo Expo: Power for Land, Sea, and Air*. 45769: American Society of Mechanical Engineers: p. V07AT31A008. (2014).
- Tai, X. et al. Stability and steady-state response analysis of a single rub-impact rotor system. *Arch. Appl. Mech.* **85**, 133–148 (2015).
- Sinha, S. K. Rotordynamic analysis of asymmetric turbofan rotor due to fan blade-loss event with contact-impact Rub loads. *J. Sound Vib.* **332** (9), 2253–2283 (2013).
- Li, B. et al. Rotating blade-casing rubbing simulation considering casing flexibility. *Int. J. Mech. Sci.* **148**, 118–134 (2018).
- Guo, X. et al. A dynamic model for simulating rubbing between blade and flexible casing. *J. Sound Vib.* **466**, 115036 (2020).
- Sun, Q. et al. Comparison of rubbing induced vibration responses using varying-thickness-twisted shell and solid-element blade models. *Mech. Syst. Signal Process.* **108**, 1–20 (2018).
- Zeng, J. et al. Rubbing response comparisons between single blade and flexible ring using different rubbing force models. *Int. J. Mech. Sci.* **164**, 105164 (2019).
- Zeng, J. et al. Rubbing dynamic characteristics of the blisk-casing system with elastic supports. *Aerosp. Sci. Technol.* **95**, 105481 (2019).
- Zeng, J. et al. Dynamic response characteristics of the shaft-blisk-casing system with blade-tip rubbing fault. *Eng. Fail. Anal.* **125**, 105406 (2021).
- Li, Y. et al. Rub-impact dynamic analysis of a dual-rotor system with bolted joint structure: theoretical and experimental investigations. *Mech. Syst. Signal Process.*, **209**, 111144 (2024).
- Hong, J. et al. *Research on Blade-Casing Rub-Impact Mechanism by Experiment and Simulation in Aeroengines*. Shock and Vibration, 2019:3237960. (2019).
- Jin, M. The nonlinear dynamic characteristics of the aero-turboshaft engine rotor blade casing rubbing system with the curvic couplings considering the elastoplastic stage. *Eng. Anal. Boundary Elem.* **161**, 78–102 (2024).
- Duchemin, M., Berlioz, A. & Ferraris, G. Dynamic behavior and stability of a rotor under base excitation. *J. Vib. Acoustics-Transactions Asme.* **128** (5), 576–585 (2006).
- Sousa, M. S. et al. Numerical and experimental investigation of rubbing existence in the context of a rotating machine under base excitation. *J. Vib. Acoust.*, **147**(4), 041001 (2025).
- Dakel, M., Baguet, S. & Dufour, R. Steady-state dynamic behavior of an on-board rotor under combined base motions. *J. Vib. Control.* **20** (15), 2254–2287 (2014).
- Gao, T. et al. An experimental study on the nonlinear vibration phenomenon of a rotor system subjected to barrel roll flight and coupled rub-impact faults. *Measurement*, **153**, 107406 (2020).
- Zheng, N. et al. *Coupled Lateral and Torsional Vibration of Rub-Impact Rotor during Hovering Flight* (Shock and Vibration, 2021). 2021(1).
- Wang, Q. et al. Rubbing vibration characteristics of double-rotor system under wave load. *J. VibroEng.* **25** (1), 1–14 (2022).
- Liu, Z. et al. *Dynamics response of an on-board rotor supported on modified oil-film force considering base motion*. Proceedings of the Institution of Mechanical Engineers, Part C: Journal of Mechanical Engineering Science, 232(2): pp. 245–259. (2018).
- Zhang, L. et al. Vibration analysis of coupled bending-torsional rotor-bearing system for hydraulic generating set with rub-impact under electromagnetic excitation. *Arch. Appl. Mech.* **86** (9), 1665–1679 (2016).
- Wang, J. et al. Transient state analysis of a rub-impact rotor system during maneuvering flight. *Chin. J. Aeronaut.* **37** (7), 236–251 (2024).
- Qi, W. et al. Investigation on the characteristics of rub-impact and misalignment faults in aero-engines during diving-climbing maneuver. *J. Sound Vib.* **606**, 119019 (2025).

29. Lin, R. et al. *Nonlinear Vibration and Stability Analysis of an aero-engine dual-rotor System Subjected To high-frequency Excitation* (Chinese Journal of Aeronautics, 2025).
30. Zhang, H. et al. Analysis of Unbalance Response and Vibration Reduction of Aeroengine Gas Generator Rotor System. *Lubricants*, **13**(6), 266 (2025).
31. Zhang, H. et al. *Dynamic Modeling and Vibration Characteristic Analysis of Fiber Woven Composite Shaft–Disk Rotor with Weight-Reducing Holes*. *Applied Sciences*, **14**(19) (2024).

## Acknowledgements

The authors would like to thank the anonymous reviewers for their very valuable comments.

## Author contributions

Haibiao Zhang: Writing – original draft, Validation, Software, Methodology, Investigation. Tao Liu: Writing – review & editing, Validation, Investigation, Funding acquisition. Haifeng Zhao: Writing – review & editing. Qingshan Wang: Writing – review & editing, Conceptualization.

## Funding

This paper is supported by the Postdoctoral Fellowship Program of CPSF under Grant Number GZC20250921 and the China Postdoctoral Science Foundation-Hunan Joint Support Program under Grant Number 2025T005HN.

## Declarations

### Competing interests

The authors declare no competing interests.

### Additional information

**Correspondence** and requests for materials should be addressed to T.L.

**Reprints and permissions information** is available at [www.nature.com/reprints](http://www.nature.com/reprints).

**Publisher's note** Springer Nature remains neutral with regard to jurisdictional claims in published maps and institutional affiliations.

**Open Access** This article is licensed under a Creative Commons Attribution-NonCommercial-NoDerivatives 4.0 International License, which permits any non-commercial use, sharing, distribution and reproduction in any medium or format, as long as you give appropriate credit to the original author(s) and the source, provide a link to the Creative Commons licence, and indicate if you modified the licensed material. You do not have permission under this licence to share adapted material derived from this article or parts of it. The images or other third party material in this article are included in the article's Creative Commons licence, unless indicated otherwise in a credit line to the material. If material is not included in the article's Creative Commons licence and your intended use is not permitted by statutory regulation or exceeds the permitted use, you will need to obtain permission directly from the copyright holder. To view a copy of this licence, visit <http://creativecommons.org/licenses/by-nc-nd/4.0/>.

© The Author(s) 2025